Phase Change Heat Transfer Enhancement with Surface Modification at Atmospheric and Sub-atmospheric Pressures

by

Ayşenur ATEŞ

Submitted to the Graduate School of Natural Science and Engineering

In partial fulfillment of the requirement for the degree of

Master of Science

Sabanci University

June 2022

ABSTRACT

Phase Change Heat Transfer Enhancement with Surface Modification at Atmospheric and Sub-atmospheric Pressures

Ayşenur ATEŞ

Mechatronics Engineering, MSc. Thesis, June 2022

Thesis Supervisor: Prof. Ali KOŞAR

Keywords: Phase change, Boiling, Heat transfer enhancement, Surface modification

Surface modifications are one of the major techniques in enhancing boiling heat transfer, achievement of higher cooling performance, and energy efficiency. The surface modification can be performed with the external structures including micro pin fins or changes in surface wettability such as the use of biphilic surfaces.

The aim of the first thesis is to reveal the effects of pin fins and tip clearance as well as distribution pin fins, which served for more uniform flow distribution, on flow boiling. For this, experiments were conducted on five different heat sinks including a reference configuration (plain channel) and different elliptical pin fin and tip clearance configurations at mass fluxes of 125 kg/m^{2}s, 225 kg/m^{2}s, and 325 kg/m^{2}s within the heat flux range of 18 – 175 W/cm^2 using de-ionized water as the working fluid. Experimental flow boiling heat transfer results and performances of each heat sink were presented with the help of flow visualization. Accordingly, the maximum heat transfer performance was achieved with a pin fin heat sink with distribution pin fins and no tip clearance on the heating area. It was also proven that streamlined pin fin configurations with uniform flow distribution are helpful in enhancing the heat transfer performance in flow boiling.

In addition, pool boiling experiments were conducted to investigate the boiling heat transfer performance of surfaces with uniform (superhydrophobic and superhydrophilic) and mixed (superbiphilic) wettability. Experimental results were obtained from four different surfaces for both atmospheric (103.7 kPa) and sub-atmospheric (28.3 kPa) pressures and the wettability effect was investigated using saturated deionized water as the working fluid in the heat flux range of 7 - 290 kW/m^2. The experimental results show that the superbiphilic surface (superhydrophobic spots with a pitch size of 3 mm and diameter of 0.7 mm) offers improvements in boiling heat transfer at both atmospheric and sub-atmospheric pressures up to 98% and 54%, respectively. Due to bubble coalescence being more likely to occur at sub-atmospheric pressure, the enhancement effect of superbiphilicity on boiling heat transfer is more significant for atmospheric pressure.

ÖZET

Atmosferik ve Altmosferaltı Basıçlarda Yüzey Modifikasyonları ile Faz Değişim Isı Transferinin İyileştirmesi

Ayşenur ATEŞ

Mekatronik Mühendisliği Yüksek Lisans Tezi, Haziran 2022

Tez Danışmanı: Prof. Ali KOŞAR

Anahtar Kelimeler: Faz değişimi, Kaynama, Isı transfer iyileştirmesi, Yüzey modifikasyonu

Yüzey modifikasyonları, kaynama ısı transferi arttırmada, daha yüksek soğutma performansı elde etmede ve enerji verimliliğini geliştirmede önemli yöntemlerden biridir. Yüzey modifikasyonu mikro pin finler gibi harici yapıların varlığı veya bifilik yüzeylerle olduğu gibi yüzey ıslanabilirliğindeki değişiklikler ile oluşur.

Bu tezin amacı, harici bir yapı olan pin finlerin, uç açıklığının, ayrıca daha homojen akış dağılımı sağlayan dağıtım görevi gören pin finlerinin akış kaynama üzerindeki etkisini ortaya koymaktır. Bu amaç doğrultusunda, deneyler referans konfigürasyon (düz kanal) ve farklı boyutlardaki eliptik pin finlerin ve uç açıklığını içeren beş farklı soğutucu üzerinde 125 kg/m^{2}s, 225 kg/m^{2}s, ve 325 kg/m^{2}s kütle akısında ve 18 – 175 W/cm^2 ısı akısı aralığında çalışma sıvısı olarak deiyonize su kullanılarak gerçekleştirilmiştir. Deneysel akış kaynama ısı transferi sonuçları ve herbir soğutucunun performansı akış görselleştirmesi yardımıyla ortaya konulmuştur. Buna göre, maksimum ısı transfer performansı ısıtma alanında pin fin uç açıklığı olmayan soğutucuda gözlemlenmiştir. Aynı zamanda homojen ısı dağılımına sahip aerodinamik pin fin yapılarının akış kaynama

ısı transfer performansını artırmada yardımcı olduğu kanıtlanmıştır.

Ayrıca, havuz kaynama deneyleri kaynama ısı transfer performansını araştırmak için tek tip (süperhidrofilik ve süperhidrofobik) ve birleşik (süperbifilik) ıslanabilirlik özelliğine sahip yüzeylerde incelemek için gerçekleştirilmiştir. Bu tez dört farklı yüzeyden atmosferik (103.7 kPa) ve atmosferaltı (28.3 kPa) basınçlardan elde edilen sonuçları sunmakta ve çalışma sıvısı olarak doymuş deiyonize su kullanılarak 7 - 290 kW/m^2 aralığındaki ısı akısında ıslanabilirliğin etkisinin anlaşılmasını amaçlamaktadır. Deneysel sonuçlara göre superbifilik yüzey (adım boyutu 3 mm ve çapı 0.7 mm süperhidrofobobik noktalar) hem atmosferik hem de atmosferaltı basınçlarda ısı transferinde sırasıyla %98 ve %54 gelişme sağlamıştır. Kabarcık birleşmesinin atmosferaltı basınçta meydana gelme olasılığının daha yüksek olması nedeniyle, süperbifilik özelliğin kaynama ısı transferindeki artırıcı etkisi atmosferik basınçta daha baskındır.

Acknowledgments

Firstly, I would like to thank my advisor Prof. Ali Koşar, who always guide me throughout my master journey. I felt his unconditional support and encouragement every step in this study. He changed my research objectives, and he shaped my academic perspectives. He taught me how I can be stronger. I will never forget his support.

I would like to thank my lovely teacher Prof. Sadık Kakaç. He always pushes me to achieve success. His unconditional support will be always remembered.

I would like to thank my jury members Prof. Burç Mısırlıoğlu and Yegan Erdem for their time and comments. Special thanks to Prof. Burç Mısırlıoğlu for his supports and valuable advices throughout this journey.

I would like to thank Sabanci University and Sabanci University Nanotechnology Research and Application Center for providing equipment. Especially, Süleyman Çelik, who always helps me, and I will always remember our scientific discussions.

I have spent a lot of time in the Micro-Nanoscale Heat Transfer and Microfluidic Laboratory at Sabanci University, I will always miss my laboratory and equipments.

I would like to thank ASELSAN company to support this thesis and our colleagues Dr. Murat Parlak, Vedat Yağcı, and Muhammed Çağlar Malyemez.

I would like to thank TUBITAK for supporting this thesis and for financial support throughout my master degree.

I would like to thank the co-authors of the articles.

I would like to thank Dr. Morteza Ghorbani and Dr. Merve Zuvin.

I would like to thank Zülal Muganlı for her support, friendship, and love throughout this journey. I do not know how I could complete this journey without her existence. Her friendship will always be remembered, and I will always be there for her. I will miss her wherever I go..

I would like to thank Dr. Ghazaleh Gharib for her valuable support and love throughout this journey. Her advice makes me always strong. She was my big sister. I will miss her so much.

I would like to thank my friends Sümeyra, Farzad, Kaveh, Araz, Amin, Ali Rashed, Rana, Arash, Eda, Saher, Vahid, İsmail, İlayda, Alp, Gamze, Osman, İrem, Alperen, Naimeh, Zahra, Faraz, Sayedali, Mohammodamin, Akam, Jalal, Mandana, Pariya, Abdülmecit, Pouya, Tayfun for their friendship and support.

I would like to thank Saltuk for his existence. There is no word to define his means for

me. His support and love make me always strong. He pushed me so hard to achieve every success that I had. This journey cannot be completed without his support. We will continue our dreams together.. The new chapter of our life will start soon. I will always be there for him.

I would like to thank my lovely family for their endless love, support, and everything. I love you so much. Especially, my niece Nehir Meyra and my nephew Kayra.. You are growing so fast.. Your auntie will always be there for you..

Remember to look up at the stars and not down at your feet. Try to make sense of what you see and wonder about what makes the universe exist. Be curious. And however difficult life may seem, there is always something you can do and succeed at.

<div align="right">

Stephen Hawking

</div>

Table of Contents

List of Tables

List of Figures

Nomenclature

a	Width of the channel (m)
A	Heated surface area (m)
A_{fin}	Total fin surface area (m^2)
A_{base}	Base area of heater (m^2)
$A_{c,fin}$	Cross – sectional area of pin fins (m^2)
A_{min}	Minimum cross-sectional area of channel (m^2)
A_t	Total heat transfer area (m^2)
b	Height of the channel (m)
Bo	Boiling number $\left(\frac{q_w''}{Gh_{fg}}\right)$
c_p	Specific heat $(J.kg^{-1}.K^{-1})$
C_{sf}	Surface constant
g	Gravitational constant $(m.s^{-2})$
H	Height of the liquid inside the boiling chamber (m)
h_{fg}	Latent heat of working fluid
k_{fluid}	Thermal conductivity of the fluid $(W.m^{-1}.K)$
l_{al}	Distance between the T₁ and aluminum heater surface (m)
L	Length of the channel (m)
$\dot{m}$	Mass flow rate $(kg.s^{-1})$
Nu_{ave}	Average Nusselt number
Nu	Nusselt number
$N_{t,fin}$	Total number of pin fins
P	Electrical power (W)
p	Pressure (kPa)
P_{fin}	Perimeter of elliptical pin fin (m)
P_s	System pressure (kPa)
P_{sat}	Head pressure (kPa)
Pr	Prandtl number
S_L, c	Longitudinal pitch of circular pin fin (mm)
S_L, e	Longitudinal pitch of elliptical pin fin (mm)

S_T, c	Transverse pitch of circular pin fin (mm)
S_T, e	Transverse pitch of elliptical pin fin (mm)
q''	Heat flux ($W.m^{-2}$)
$\dot{Q}$	Energy Transferred (W)
Q_{loss}	Heat loss (W)
$\dot{Q}_{loss,tp}$	Heat loss in two - phase experiments (W)
$R_{conduction}$	Conductive thermal resistance ($K.W^{-1}$)
$R_{convection}$	Convective thermal resistance ($K.W^{-1}$)
$R_{caloric}$	Liquid caloric thermal resistance ($K.W^{-1}$)
R_{total}	Total thermal resistance ($K.W^{-1}$)
R_{tp}	Thermal resistance of thermal paste ($K.W^{-1}$)
Re	Reynolds number
t_{al}	Thickness of aluminum plate (m)
ΔT	Wall superheat (K)
T_1	Temperature on the exact location of the aluminum heater (K)
$T_{av,surface}$	Average surface temperature (K)
$T_{av,fluid}$	Average fluid temperature (K)
$T_{av,wall}$	Average wall temperature (K)
T_{inlet}	Inlet temperature of fluid (K)
T_{outlet}	Outlet temperature of fluid (K)
T_s	Surface temperature (K)
T_{sat}	Saturation temperature of fluid (K)
T_w	Wall temperature (K)
$T_{x,surface}$	Surface temperature at exact location (K)
U_{ai}	Uncertainty
V	Voltage (V)
w	Width of the channel (m)
Greeks	
η_{pin}	Pin Fin effectiveness
μ	Dynamic viscosity of fluid ($Pa.s$)
ρ_f	Water density at exact pressure ($kg.m^{-3}$)

ρ_l	Density of liquid phase of working fluid ($kg.m^{-3}$)
ρ_v	Density of vapor phase of working fluid ($kg.m^{-3}$)
Subscript	
sat	Saturated
W	Wall
D	Distribution Pin Fin

1. CHAPTER 1: INTRODUCTION

1.1. Background

Over the decades, researchers have aimed to increase in heat removal rate using modified surfaces such as pin finned structures and surface functionalization (changing the water contact angle). However, there are some challenges to provide high heat flux cooling from the surfaces. There is an urgent need to increase the heat transfer rate on miniaturized systems.

The researchers tend to increase the performance in microelectronic devices by adding transistors onto chips. However, this results in high heat generation which necessitates effective and reliable operation. Boiling is an effective heat transfer mechanism for ultra high heat flux cooling and fulfilling the needs in microelectronics. This constitutes the motivation in this thesis.

1.1.1. Fundamentals of boiling

Boiling includes phase change from liquid to gas and occurs when the bulk liquid reaches saturation temperature a specified pressure as well as under conditions where the wall temperature is above the saturation temperature. This temperature difference leads to the formation of bubbles on the heating surface.

There are known two types of boiling, namely flow boiling and pool boiling. Flow boiling occurs when a fluid flows over a heated surface. On the other hand, pool boiling occurs when a large volume of stagnant liquid is heated from a submerged heated surface. Three major types of boiling heat transfer mechanisms can be characterized as nucleate boiling, convective boiling, and film boiling. Nucleate boiling can be detected when the tiny bubble formation occurs and departs from the heated surface. On the other hand, convective boiling where heat is conducted through a thin liquid layer that evaporates at the liquid-vapor interface visible. Furthermore, in film boiling, a vapor film covers the heated surface, and heat is transferred by conduction and radiation.

1.1.2. Literature review on pin finned surfaces in micro/minichannels

Energy efficiency and the development of alternative energy sources are among the most pressing challenges of the twenty-first century. The development of energy-efficient miniaturized systems has become one of the key topics. Miniaturization has influenced heat exchanger technology, which is vital in miniature thermal-fluids and microfluidic systems. The efficiency of a heat exchanger has a significant impact on the overall efficiency of these systems [1,2].

In most cases, generated heat in microprocessors is transmitted to a heat sink via heat conduction and subsequently via natural, mixed, or forced convection to the environment. As the temperature increases, heat sinks with low heat removal efficiency are not capable of preventing serious damage to microelectronic components. Furthermore, air cooling fails to satisfy the requirements for high-density heat dissipation. As a result, new generation heat sinks should be suitably developed to enhance heat removal rates to prevent miniaturized devices from overheating. An efficient thermal management system with effective heat sinks is a major objective in this regard, which was also rigorously investigated [3–10]. Optimization of heat sink design with the aim of enhancing fluid-structure interactions is a common thermal management approach. One of these promising enhancement methods is the use of pin fins to promote the flow boiling performance, which was extensively covered in the literature [11–15]. Furthermore, pin fins interrupt the flow, break down the boundary layer, and lead to the regeneration of thermal and hydraulic boundary layers [16,17].

Flow boiling heat transfer in small channels is one of the major approaches in effective heat dissipation. During two-phase boiling flow in microchannels, the surface plays an important role in bubble behavior including bubble nucleation, detachment, and movement, and also influencing flow boiling heat transfer. Micro pin fins are one of the leading alternatives for promoting flow boiling. Therefore, some studies utilized pin fins to improve heat transfer performance because of their significant benefits in flow boiling as well as their great potential in heat dissipation [5,11,12,18,19]. In addition, the geometrical design of microchannels has also a significant impact on the flow boiling heat transfer performance [7].

The pin fin implementation to microchannel heat sinks introduces significant benefits in single-phase flows and flow boiling. So far, various pin fin configurations including

square, circular, rectangular, plate, elliptical, and triangular pin fins have been considered in both experimental and numerical studies [16,18,20–24]. As an example, by analyzing an inline arrangement of three fins, Ricci and Montelpare [25] explored the effect of fin cross-sectional shape on the thermal efficiency of a water-cooled pin-fin heat sink. Their findings revealed a stronger relationship between Nusselt number and fin shape and location, and the triangular and rhomboidal fins outperformed the other fin forms (circular, square, triangular, and rhomboidal) in terms of heat transfer.
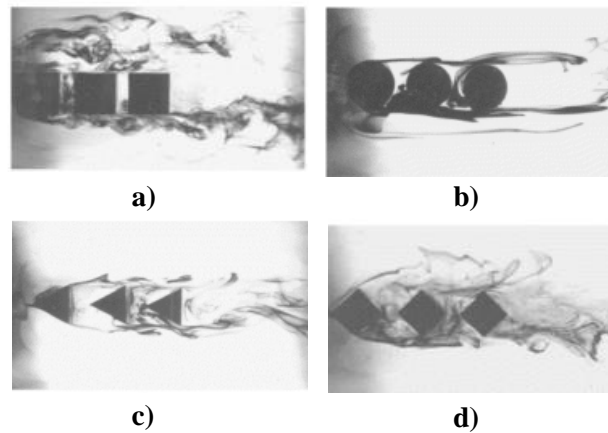
Figure 1 Different shape of pin fin structures a) square b) circular c) triangular d) rhomboidal. [25].

Koşar and Peles [26] experimentally examined the pressure drop and heat transfer characteristics of water-cooled pin-fin heat sinks by analyzing staggered arrangements of circular, hydrofoil, rectangular, and cone-shaped pin-fins. At a low Reynolds number and pressure drop, streamlined pin-fins increased the performance of the heat sink. In a numerical study, Bai et al. [27] reported the entrance effect of ribs disrupted in a pin-fin array. The entry effect improved total heat transfer while simultaneously reducing the pressure drop of the pin-fin array, thereby resulting in a higher thermal efficiency. In the literature, while there are numerous studies on pin fin heat sinks based on many parameters such as pin-fin shape, arrangement, tip clearance, flow velocity, and distribution [28–36], there are limited studies on elliptical shape pin fins [20,37,38], which offer a large surface area along with reduced pressure drop due to their streamlined geometry.

Moreover, some limited experimental and numerical studies reported that tip clearance decreased the cooling performance of a heat sink. As a result, optimization studies on

3

minimizing the thermal resistance of microchannel heat sinks proposed only cases, where there was no tip clearance [39–41]. Yim Min et al. [42] reported that when the tip clearance was less than the channel width, the cooling performance of a microchannel heat sink could be improved. In another study, Moores and Joshi [43] reported that the tip clearance smaller than 10% of the pin fin height resulted in a better performance. In another study, Shahsavar et al. [44] reported the impact of tip clearance on a pin fin heat sink by using CFD (Computational Fluid Dynamics) simulations. The results demonstrated that removing the tip clearance reduced the convective heat transfer coefficient because the velocity intensification decreased.

1.1.3. Literature review on uniform and mixed wettable surfaces in boiling at atmospheric and sub-atmospheric pressure

Boiling heat transfer coefficient (HTC) is affected by surface properties such as the roughness, porosity, and wettability of the surface in the nucleate boiling regime. Several studies have proven the effects of macrostructure on the parameters of vapor-liquid two-phase flows near a heating surface, which lead to heat transfer enhancements [45,46].

By changing the mass and momentum transfer between liquid and vapor phases at the three-phase contact line [47], surface wettability affects bubble nucleation, bubble dynamics and resultant heat transfer rate as well as critical heat flux [48]. The effect of surface wettability on surfaces with coatings was investigated by numerous studies in the literature. As an example, Coyle et al. [49] proposed surfaces having mixed wettability with various hydrophobic and hydrophilic patterns to study the effect of surface biphilicity on CHF and HTC in pool boiling at atmospheric pressure. They achieved enhancements between 50% and 90% in CHF compared to the bare surface. Hsu et al. [50] reported CHF enhancement up to 100% on superhydrophilic surfaces coated with silica nanoparticles compared to the plain surface. Their results presented an increase in CHF for surfaces with lower static contact angle values. In another study, Betz et al. [14] fabricated surfaces with various wettability characteristics. Single bubble departure was reported as a function of superheat for the hydrophobic and superhydrophobic surfaces due to the bubble merging. In comparison to the hydrophobic surface, the hydrophilic surface had smaller HTCs at lower wall superheats but larger HTCs at higher wall superheats [51]. Surtaev et al [52] investigated the influence of the surface wettability on

local boiling characteristics and HTC at various sub-atmospheric pressures (11.3-102.8 kPa) when the boiling behavior on conventional hydrophilic surfaces significantly changes. In particular, it was shown that on a hydrophobic surface, with decreasing pressure, the bubble emission frequency increases, and bubble departure diameter practically does not change, which differs significantly from the behavior of these characteristics with pressure during boiling on a hydrophilic surface. Moreover, it was discovered that the usage of hydrophobic coatings led to an enhancement of heat transfer at low heat fluxes and low pressures although CHF decreases with pressure reduction.
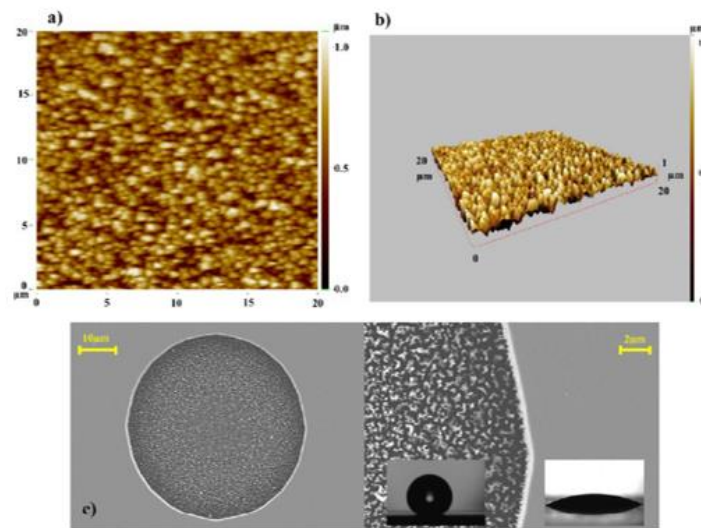
Figure 2 Fabricated biphilic surface for pool boiling enhancement at atmospheric pressure a) AFM result 2D, b) AFM result 3D, c) SEM image and contact angle measurement results [53].

A number of studies in the literature have shown significant increases in HTC using biphilic surfaces at atmospheric pressure [54,55]. Accordingly, some studies on biphilic surfaces [56] reported larger HTCs compared to the unmodified [57] and nanostructured [58] surfaces. Obtained results from available studies also suggest that the heat transfer performance depends on the ratio of hydrophobic to the hydrophilic area for biphilic surfaces compared to the bare surfaces with uniform wettability. Motezakker et al. [53] defined A* as the ratio of the hydrophobic area to the total surface area for biphilic surfaces and proposed an optimum ratio of 38.46% that offered the best boiling performance in terms of heat transfer coefficient and CHF in pool boiling at atmospheric pressure (Figure 2). It was observed that CHF increased with the extent of the

hydrophobic region compared to a hydrophilic region at atmospheric pressure in pool boiling. At atmospheric pressure, hydrophobic regions have a better performance than hydrophilic areas at low heat fluxes due to the larger number of active nucleation sites and earlier onset of nucleate boiling [53].
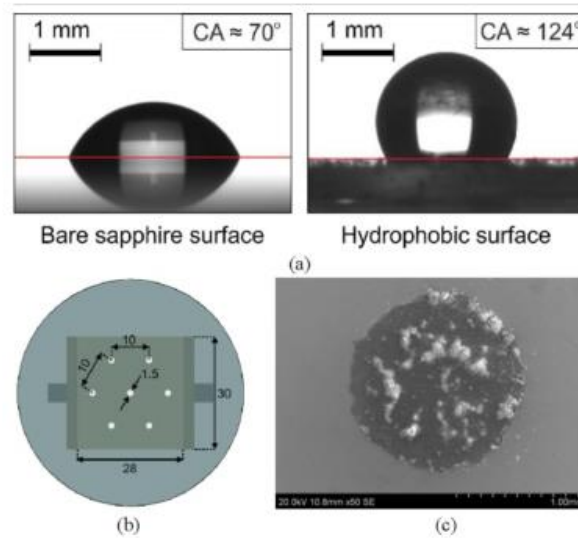
Figure 3 Fabricated biphilic surface for pool boiling enhancement at sub-atmospheric pressure a) contact angle measurement, b) schematic of biphilic configuration, c) SEM image of individual hydrophobic spot [48].

From the above-mentioned studies, it can be realized that biphilic surfaces can combine the advantages of hydrophilic and hydrophobic surfaces [59–61]. Accordingly, on such surfaces, hydrophobicity is present to promote bubble nucleation and enhance heat transfer, while hydrophilicity ensures liquid transport to the surface in the regime of slugs and vapor columns, resulting in extending CHF [62]. As an example, Ahmadi et al [54] tested surface samples with hydrophobic and hydrophilic zones and three regions with various hydrophobicity ratios in a high aspect ratio microchannel. According to their results, biphilic surfaces could achieve enhancements up to 56.7% in heat transfer compared to the reference hydrophilic sample [54].

Applications such as adsorption heat pumps, seawater desalination, and modern cooling systems could benefit from boiling at sub-atmospheric pressures [63–65]. Therefore, boiling heat transfer at sub-atmospheric pressures has become an emerging research topic in boiling heat transfer. The system pressure is one of the parameters having a significant impact on bubble nucleation, heat transfer rate, and critical heat flux in nucleate boiling [49,66]. The nucleation site density and bubble departure frequency decrease upon a

reduction in the system pressure, thereby resulting in larger bubble departure diameters. Surface modification is one of the major approaches that can be used as an effective method to obtain the desired bubble nucleation and growth when operating at sub-atmospheric pressures and to address the challenges in boiling at sub-atmospheric pressures [67–69].

1.2. Motivation and Novel Aspects

From the literature review, it is clear that natural and forced air convection systems are not enough for the high heat flux cooling applications. Therefore, there is a need for novel cooling strategies in boiling surface modification in both flow and pool boiling. In this thesis, the potential cooling systems experimentally studied for future applications.

In this thesis, the effects of pin fins, distribution pin fins, and tip clearance on flow boiling were explored at three different mass fluxes. Five different heat sinks including reference configuration (plain channel), different elliptical pin fin, distribution pin fin, and tip clearance configurations were tested. Moreover, heat transfer and visualization results in designed and fabricated heat sinks were presented to explain the trends in the thermal performance. From obtained results, heat transfer enhancements up to 36% could be achieved with elliptical pin fins. Moreover, distribution pin fins can further augment heat transfer. Elliptical pin fins without tip clearance lead to the best performance and the transition between flow patterns is delayed with the presence of pin fins.

In second study, although there are several studies on the effects of surface wettability on boiling heat transfer at atmospheric pressure, few research efforts exist at sub-atmospheric pressures, particularly for surfaces with mixed wettability. This study aims to investigate the boiling phenomenon on surfaces with uniform (superhydrophilic and superhydrophobic) and mixed (superbiphilic) wettability at both atmospheric and sub-atmospheric pressures. This study includes experimental results obtained from four different surfaces and reveals the effect of surface wettability on boiling heat transfer at sub-atmospheric pressure. From obtained results, superbiphilic surface offered improvements at both atmospheric and sub-atmospheric pressures. The enhancement effect of superbiphilicity on boiling heat transfer is more significant for atmospheric pressure. Superhydrophobic island pitch size had a negligible effect on boiling heat transfer at atmospheric pressure.

1.3. Thesis Objectives

This study aims to reveal the effect of surface modification and wettability in both flow and pool boiling. Two studies were performed to reveal the boiling heat transfer performance and mechanisms on modified surfaces:

- Flow boiling heat transfer on modified surfaces:
  - Investigation on heat transfer performance in the presence of elliptical pin fins.
  - Examination of flow boiling heat transfer in the presence of distribution (circular) pin fin.
  - Revealing tip clearance effect (0 mm, 1 mm, and 2 mm).
- Pool boiling heat transfer on modified surfaces:
  - Investigation effect of surface wettability effect (homogenous superhydrophilic, homogenous superhydrophobic, and superbiphilic) at atmospheric and sub-atmospheric pressure in pool boiling.
  - Offering a novel fabrication approach to obtain mixed wettability.
  - Investigating the heat transfer performance and mechanisms on modified surfaces at both atmospheric and sub-atmospheric pressures.

2. CHAPTER 2: FLOW BOILING HEAT TRANSFER ON MODIFIED SURFACES

2.1. Objectives

This study aims to reveal the effects of pin fins, distribution pin fins, and as well as tip clearance at three different mass fluxes in flow boiling. For this reason, five different heat sinks were fabricated and used on flow boiling experiments. The heat transfer and visualization results were presented.

2.2. Experimental Method

2.2.1. Heat Sink Design, Fabrication, and Package

To conduct flow boiling experiments, five heat sink configurations were designed and fabricated. The configurations (test section) have a width of 34 mm and a length of 74.56 mm. The outer wall thickness is 10 mm to include screws and O-rings for each configuration. The configurations were designed as a small channel with the same width (4 mm) and length (14.56 mm). Elliptical pin fins were used (Configuration #2, #3, #4, #5) along the heating area, while circular pin fins were used for flow distribution (Configuration #3, Configuration #4, and Configuration #5) at the inlet. To obtain experimental results, the configurations were fabricated, and different heights of pin fins (1 mm, 2 mm, and 3 mm) were used for each configuration. Configuration #1 does not have any pin fin and served as a reference. Configuration #2 without distribution pin fins has a pin fin height of 2 mm over the pin finned area, and the others (Configuration #3, Configuration #4, and Configuration #5) have distribution pin fins (3 mm height) and pin finned area with elliptical pin fins of different pin fin heights to provide three different

clearances (Figure 4).
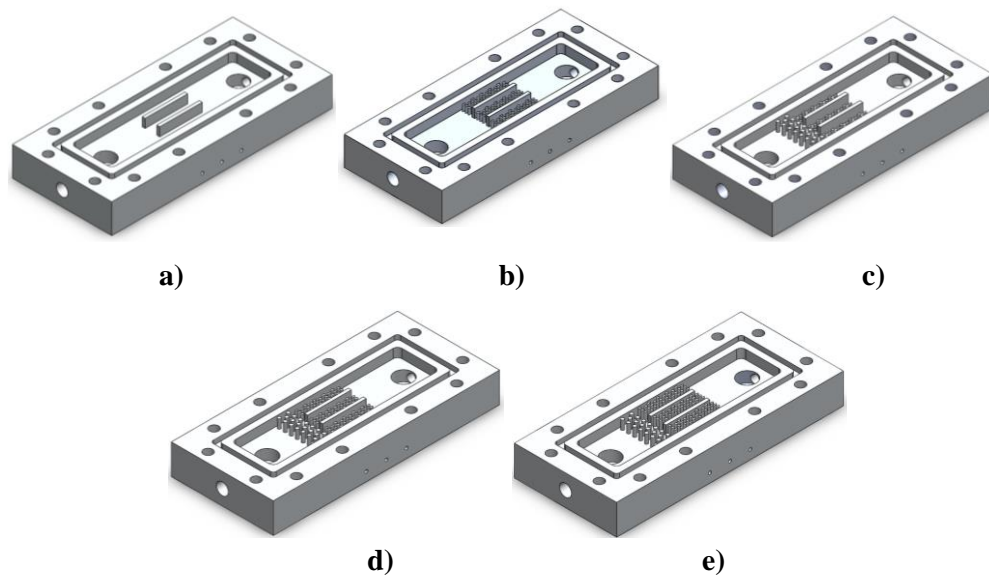
Figure 4 CAD model of fabricated configurations a) Configuration #1 (reference plate), b) Configuration #2, c) Configuration #3, d) Configuration #4, and Configuration #5.

The configurations are displayed in Figure 5. Furthermore, Table 1 summarizes the details about each configuration. The channel includes 10 and 3 rows of staggered elliptical pin fins and staggered (distribution) circular pin fins for each configuration (Configuration #3, Configuration #4, Configuration #5), respectively. As stated before, Configuration #2 has only a staggered elliptical pin finned area. Total numbers of elliptical pin fins and circular pin fins (distribution of pin fins) are 90 and 20, respectively. The pitch ratio of

elliptical pin fins and circular pin fins (distribution pin fins) is 1.5.
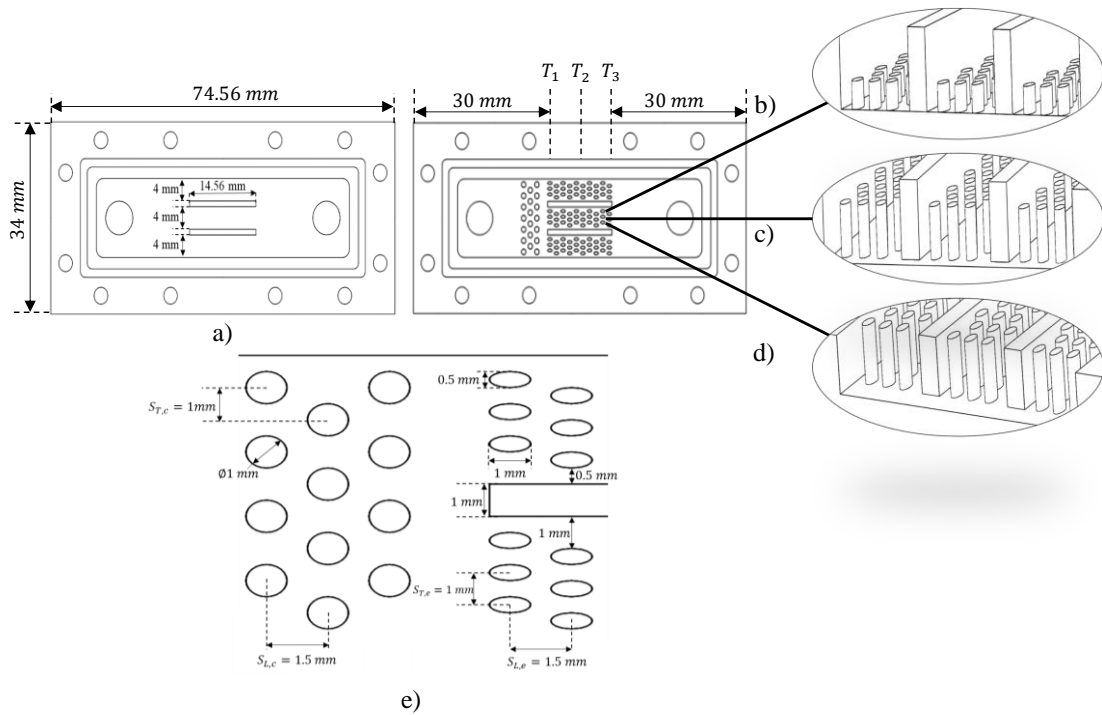
Figure 5 CAD design images a) without pin finned area (Configuration #1),
b) 2 mm tip clearance (Configuration #3), c) 1 mm tip clearance (Configuration #4), d)
no tip clearance (Configuration #5), and e) dimensions of distribution pin fins and
elliptical pin fins (base area).

Three thermocouple holes were located on each plate to obtain accurate temperature results at the inlet of the elliptical pin finned area (T_1), middle of the elliptical pin finned (T_2) and end of the elliptical pin finned area (T_3). Each configuration was made of Aluminum 6061 and was fabricated using the CNC (Computer Numerical Control) machining processes to have a smooth surface since aluminum is preferred in the industry due to its high machinability, high thermal conductivity, and smoothness. After the fabrication processes, surface roughness was measured at six locations on each configuration using the 'Mahr, MarSurf M400 Surface Roughness Tester' equipment. The probe of equipment was used on the surface near the channel, and the average surface roughness was obtained as the average of measured data points. The measured average surface roughness as a result of CNC machining was $R_a =\sim 0.25\ \mu m$ for each configuration.

Table 1 The characteristics of the fabricated configuration.

CONFIGURATIONS	
Configuration W (#1)	No pin fins, plane channels (includes 3 channels with a width of 4 mm and height of 3 mm)
Configuration W + Pin Fin (2 mm) (#2)	Totally 90 elliptical pin fins (height of 2 mm) between the walls (tip clearance of 1 mm)
Configuration W + D + Pin Fin (1 mm) (#3)	Totally 20 distribution (circular) pin fins (height of 3 mm) + Totally 90 elliptical pin fins between the walls (pin fin height of 1 mm) (tip clearance of 2 mm)
Configuration W + D + Pin Fin (2 mm) (#4)	Totally 20 distribution (circular) pin fins (height of 3 mm) + Totally 90 elliptical pin fins between the walls (pin fin height of 2 mm) (tip clearance of 1 mm)
Configuration W + D + Pin Fin (3 mm) (#5)	Totally 20 distribution (circular) pin fins (height of 3 mm) + Totally 90 elliptical pin fins between the walls (pin fin height of 3 mm) (no tip clearance)

2.2.2. Experimental Setup

An open-loop experimental setup was constructed to perform flow boiling experiments. The schematic of the setup is presented in Figure 6. The main components of the experimental setup include the inlet reservoir, pump, water bath, test section, cartridge heaters, power supply, flow meter, outlet reservoir, visualization system, and data acquisition system. Boiling images were taken by a high-speed camera, which has a full-pixel resolution of 1920x1080 at a frame rate of 3000 fps. The test section including the heat sink configurations was installed and sandwiched with the use of a transparent polycarbonate block. This transparent part allows for visualization from the top of the

configurations. O-rings were placed at the interface to prevent any leakage. To connect the test section to the water bath, suitable fittings and hoses were used. An aluminum block heater was located at the bottom side of the test section, and four cartridge heaters with a diameter of 12 mm, and a length of 75 mm were placed into the aluminum heater to obtain the desired heat flux with the use of the power supply. On the other hand, pressed configurations were sandwiched by using plexiglass to ensure that there was a direct contact between the configuration and heater's surface. Also, this heater provided conduction heating through the test section. Thermal paste was applied to reduce the thermal resistance between the aluminum block and configurations on the heating part. The reservoir was filled with degassed water, and a gear pump was used to propel degassed water through the test section. The water bath was adjusted to a suitable temperature for each mass flux to increase the fluid temperature to the saturation temperature. The inlet temperature of fluid was the same as the saturation temperature for each configuration at all mass fluxes. The outer surface of the aluminum block heater was covered by PFTE to reduce heat losses of the heating part. The flow meter was located near the outlet region of the test section for the measurement of flow rates, and pumped fluid was stored in a reservoir at the outlet. The used gear pump and hoses are durable to high temperatures.
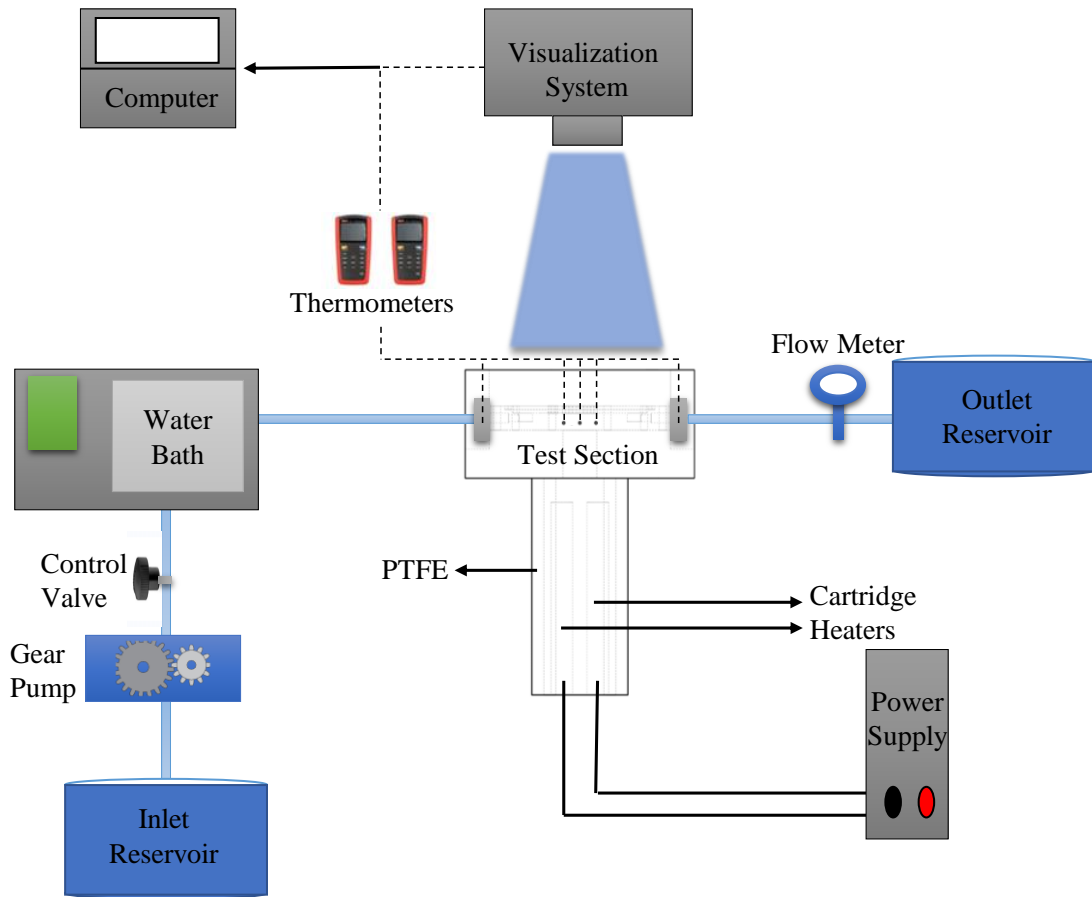
Figure 6 Schematic of the open-loop experimental setup.

2.2.3. Experimental Procedure

Before the experiments, the plates were cleaned with isopropanol. Then, the polycarbonate block was cleaned with deionized water and isopropanol to obtain a smooth and clean surface. Deionized water was used as the working fluid in the experiments. Deionized water was boiled for 30 minutes in a closed reservoir to ensure to have degassed water followed by a 10-minute waiting period in a closed inlet reservoir. This procedure was critical to obtain nucleated bubble visualization instead of gassed water. Simultaneously, the sandwiched test section was checked by using a nitrogen gun for several times to ensure that there was no leakage. Thereafter, the reservoir was located just before the pump and was connected to the setup with hoses durable over 100ºC. Before installing the test sections, the thermal paste was applied to reduce the thermal

resistance upside of the heater. While the working fluid was pumped, desired heat fluxes were applied through the test section after obtaining the flow rate stability. It was ensured that the system was under the steady-state conditions while the exit pressure was kept at the atmospheric pressure. Also, T – type thermocouples were calibrated before the tests to ensure that temperature data could be accurately obtained. Temperature data were recorded at the inlet and outlet as well as at locations on the surface for each heat flux. The experiments were repeated for several times to ensure repeatability.

2.3. Data Reduction and Uncertainty Analysis

Total power was calculated using the supplied voltage and current data. The electrical power is expressed as:

$$P = V.I \tag{1}$$

where P is the electrical power of the system, and V and I are the voltage and current values, respectively. On the other hand, heat losses $(\dot{Q}_{loss})$ were calculated by using the estimation of heat losses from the surface for boiling experiments. For this, water was evacuated, and heat was delivered to the evacuated system. Power and average surface temperature were recorded after reaching steady-state conditions. The same process was performed with the presence of water and power was applied to the system until same average wall temperature was obtained. After this procedure, linear curve was obtained in the form of $\dot{Q}_{loss,tp} = a + bT_{av,wall}$. Therefore, the maximum heat loss was found as 14.8% for boiling experiments. Furthermore, using a 1-D fin analysis with the adiabatic tip assumption, the average two-phase heat transfer coefficient can be calculated as:

$$P - \dot{Q}_{loss} = \bar{h}(\eta_{fin}N_{t,fin}P_{fin}H + wL - N_{t,fin}A_{c,fin})(T_{av,surface} - T_{sat}) \tag{2}$$

where η_{fin} is pin efficiency, $N_{t,fin}$ is the number of total elliptical pin fins for each channel, P_{fin} is the perimeter of elliptical pin fins, w is the total width of the channels, L is the length of the channel and $A_{c,fin}$ is the cross-sectional area of elliptical pin fins. Elliptical pin fin efficiency can be expressed as $\eta_{fin} = \frac{\tan mH}{mH}$ at which $m = \sqrt{\frac{\bar{h}P_{fin}}{k_{al}A_{c,fin}}}$ and H is the height of elliptical pin fin. The applied heat flux can be calculated using the net power $(P - \dot{Q}_{loss})$ the surface area of the aluminum block as:

$$q'' = \frac{(P - \dot{Q}_{loss})}{A_{base}} \tag{3}$$

To find the average surface temperature, the total thermal resistance is necessary. The conduction thermal resistance is defined as:

$$R_{conduction} = \frac{t_{Al}}{k_{Al}A_{base}} \quad (4)$$

The total area is found as:

$$A_{total} = A_{base} + \eta_{fin}A_{fin} \quad (5)$$

The convective thermal resistance is calculated as:

$$R_{convection} = \frac{1}{\bar{h}A_{total}} \quad (6)$$

The liquid caloric thermal resistance is expressed as:

$$R_{caloric} = \frac{1}{\dot{m}c_p} \quad (7)$$

The total thermal resistance is the sum of three thermal resistances:

$$R_{total} = R_{conduction} + R_{convection} + R_{caloric} \quad (8)$$

The average surface temperature can be calculated with the use of thermocouple measurements as:

$$T_{av,surface} = \frac{(T_1+T_2+T_3)}{3} - q''R_{total} \quad (9)$$

To obtain the mass flux, the mass flow rate is divided by the minimum cross-sectional flow area:

$$G = \frac{\dot{m}}{A_{min}} \quad (10)$$

where $\dot{m}$ is the mass flow rate and A_{min} stands for the minimum cross-sectional area of each channel. For the configuration #1, the total cross-sectional area was used for A_{min}. Local heat transfer coefficient is calculated based on heat flux, local surface temperature, and saturation temperature and defined as:

$$h_x = \frac{(P-\dot{Q}_{loss})}{A_{total}(T_{x,surface}-T_{sat})} \quad (11)$$

where $T_{x,surface}$ is wall temperature at the exact location. Moreover, local quality can be calculated as:

$$\chi = \frac{(P-\dot{Q}_{loss})}{\dot{m}h_{fg}}\frac{z_{th}}{L} \quad (12)$$

where z_{th} distance from the inlet at the exact location, h_{fg} is the difference of specific enthalpy values between fluid and gas state, and L is the length of the channel.
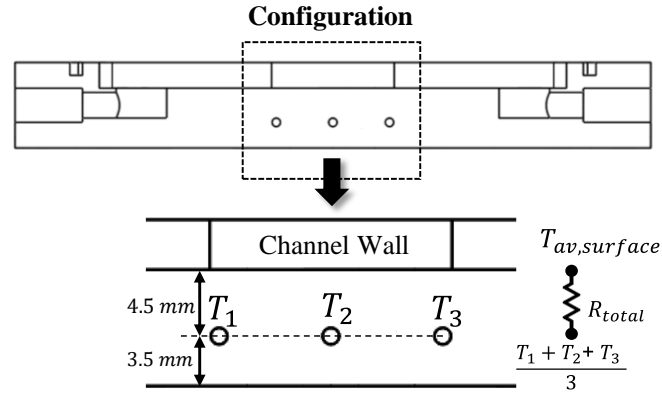
Figure 7 Schematic of thermocouple locations and approach of surface temperature measurement.

The uncertainties were obtained using the specification sheets provided by the manufacturer and the uncertainty propagation method [73]. According to this method, the uncertainty in a derived parameter can be calculated as:

$$U_p = \sqrt{\sum_{i=1}^{n} \left(\frac{\partial p}{\partial a_i} u_{ai}\right)^2} \tag{13}$$

where U_{ai} is the uncertainty in the parameter a_i. The uncertainties in major parameters are listed in Table 2.

Table 2 Uncertainties in experimental parameters.

Parameter	Uncertainty
Voltage	$\pm 1\ V$
Current	$\pm 0.01\ A$
Wall Temperature	$\pm 1 - 5\ \%$
Fluid Temperature	$\pm 1 - 4\%$
Mass Flow Rate	$\pm 3\%$
Average Heat Transfer Coefficient	$\pm 5.5\ \%$

2.4. Single – Phase Validation

Single – phase heat transfer analysis was performed to validate the experimental results before conducting flow boiling experiments. This validation was performed with the reference configuration (#1) without any pin fin. DI water was used to perform single phase heat transfer analysis. To calculate the net power, located thermocouples were used to obtain temperatures at the inlet and outlet of the configuration. This process was performed at two heat fluxes for each mass flux. Heat losses for single phase flow experiments were found using energy balance. Accordingly, the net power was calculated as:

$$\dot{Q} = \dot{m}c_p(T_{outlet} - T_{inlet}) \qquad (14)$$

The heat loss is the difference between the input power and net power and was found to be less than 10% for each mass flux. Furthermore, located thermocouples at three points (as their average) on the plate were used to obtain the wall temperature (T_{wall}). Also, the average fluid temperature was calculated. Finally, the average single – phase heat transfer coefficient is calculated as:

$$\bar{h}_{sp} = \frac{\dot{Q}}{A_{base}(T_{av,wall} - T_{av,fluid})} \qquad (15)$$

where $T_{av,fluid}$ is the average fluid temperature and can be expressed as:

$$T_{av,fluid} = \frac{T_{inlet} + T_{out}}{2} \qquad (16)$$

The single – phase average Nusselt number is defined as:

$$Nu_{ave} = \frac{\bar{h}_{sp}D_H}{k_{fluid}} \qquad (17)$$

where D_H is the hydraulic diameter and k is the thermal conductivity of the fluid. The hydraulic diameter can be found as:

$$D_H = \frac{2ab}{a+b} \qquad (18)$$

where a is the height and b is the thickness of the channel. Furthermore, the Prandtl number is defined as:

$$Pr = \frac{c_p\mu}{k_{fluid}} \qquad (19)$$

where μ is the dynamic viscosity of the fluid. Reynolds number is calculated with the knowledge of mass flux (G) and hydraulic diameter as:

$$Re = \frac{GD_H}{\mu} \qquad\qquad (20)$$

Shah and London [74] proposed a correlation to calculate average Nusselt number at uniform heat flux for thermally developing flows:

$$Nu = 1.953\left(\frac{Re.Pr.D_H}{L}\right)^{1/3} \qquad \frac{Re.Pr.D_H}{L} \geq 33.3 \qquad (21)$$

$$Nu = 4.364 + 0.0722\left(\frac{Re.Pr.D_H}{L}\right) \qquad \frac{Re.Pr.D_H}{L} < 33.3 \qquad (22)$$

Since $\frac{Re.Pr.D_H}{L} \geq 33.3$ for the experimental conditions, the first correlation was used for the validation. Figure 8 displays the comparison between the experimental data and predictions. Accordingly, the experimental data could be predicted by the correlation with a maximum error of 3.5%.
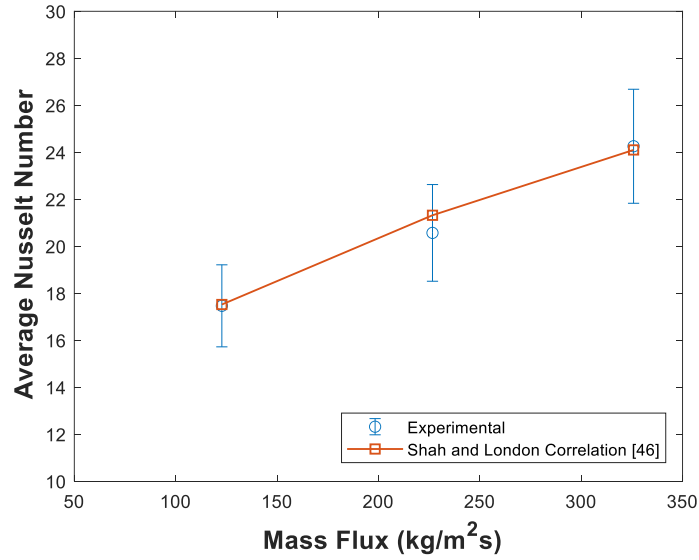
Figure 8 Comparison between the obtained experimental results and predictions of Shah and London correlation [74].

2.5. Results and Discussion

In this section, the effects of pin fins, tip clearance, and distribution pin fins on flow boiling heat transfer were discussed by displaying both boiling heat transfer and visualization results. The obtained boiling curves and HTC trends are presented for each configuration (test section) at mass fluxes of 125 kg/m^{2}s, 225 kg/m^{2}s, and 325 kg/m^{2}s in Figure 9 and Figure 10, respectively. The applied heat flux ranges from 18 W/cm^2 to 175 W/cm^2.

As can be seen from Figure 9 and Figure 10, the lowest heat flux data correspond to the conditions near boiling nucleation. It is clear that nucleate boiling is suppressed at higher heat fluxes, where the dominant heat transfer mechanism becomes convective boiling, which is supported with the presence of wavy intermittent and annular flow during flow visualization at low mass fluxes.
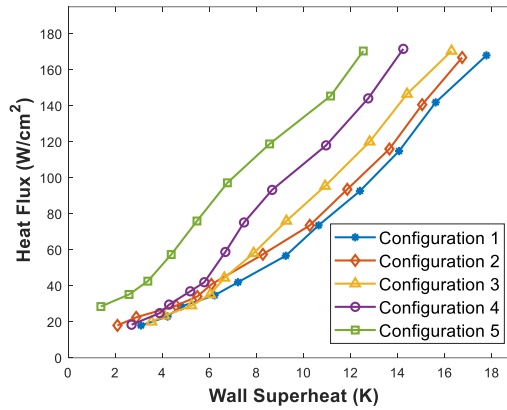
a)
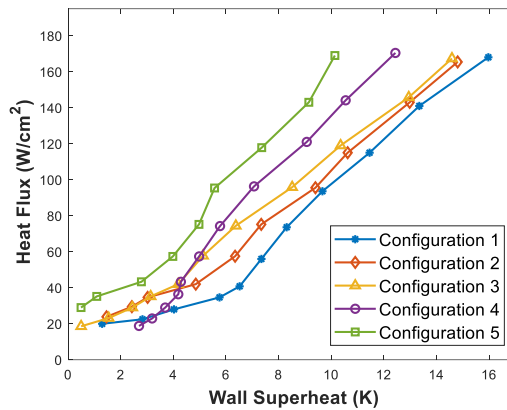
b)
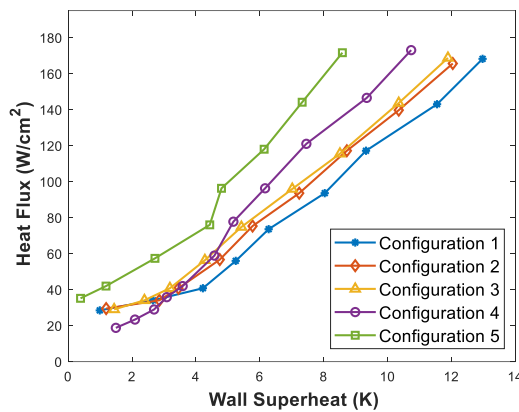
c)

Figure 9 Boiling curves for each configuration at a) G = 125 kg/m^{2}s, b) G = 225 kg/m^{2}s, c) G = 325 kg/m^{2}s.

As shown in Figure 10, Configuration #1 (with no pin fins) has the worst heat transfer performance at all mass fluxes. This is due to its minimum surface area. Configuration #2 (with only elliptical pin fins) provides enhancement in boiling heat transfer relative to Configuration #1 and provides evidence for the use of pin fins in raising the heat transfer performance. Configuration #3 (the same configuration as Configuration #2 but with distribution pin fins and with a larger tip clearance of 2 mm) exhibits a better performance than Configuration #1 and Configuration #2 at the lowest mass flux $(G = 125 \ kg/m^2 s)$. This suggests that distribution circular pin fins are effective at low mass flux in providing uniform flow distribution and in preventing the motion of vapor phase towards the inlet, which have a significant positive effect on the heat transfer performance. However, Configuration #2 and Configuration #3 have almost the same performance at higher mass fluxes (Figure 10b and c). Configuration #4 (the same configuration as Configuration #2 but with distribution pin fins) and #5 (configuration with distribution pin fins and no tip clearance) have significantly better performances than the other configurations. Configuration #5 has the best performance when considering heat transfer enhancement. Configuration #5 has a better performance up to 30%, 36%, and 35% compared to the reference plate (Configuration 1#) at the at lowest $(G = 125 \ kg/m^2 s)$, medium $(G = 225 \ kg/m^2 s)$, and highest mass flux $(G = 325 \ kg/m^2 s)$, respectively, even though the mass flow rate is 1.6 times larger for Configuration #1 at the same mass flux. This improvement is mainly due to the increase in contact surface area between solid and fluid for heat dissipation and enhanced thin film evaporation in annular flow at heat fluxes. The trends also prove that the tip clearance does not affect the heat transfer performance in a favorable way for the range of tip clearance in this study and is in good agreement with previous studies, which reported positive effects of tip clearance only at very low tip clearance values [75,76].
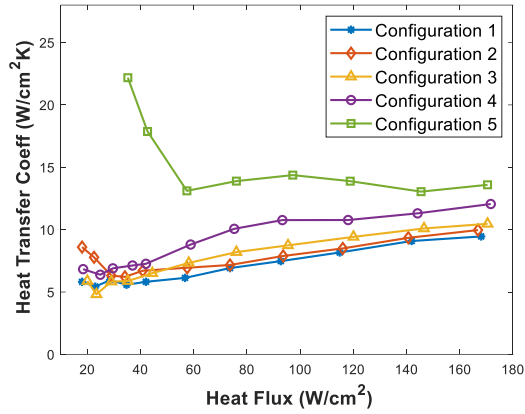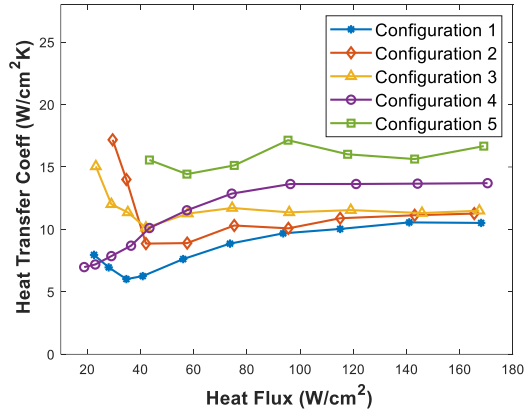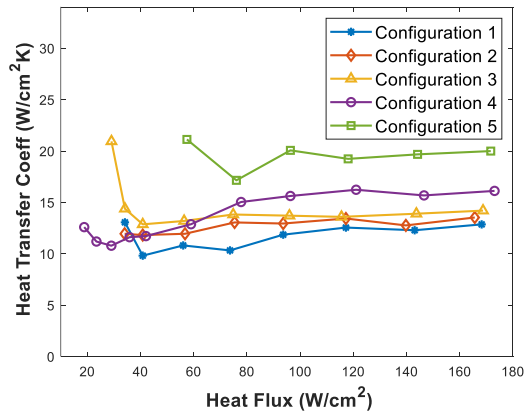
Figure 10 Two – phase heat transfer coefficient profiles for each configuration at a) G =
125 kg/m²s, b) G = 225 kg/m²s, c) G = 325 kg/m²s.

Figure 10 displays the heat transfer coefficient (HTC) profiles. As the mass heat flux increases, heat transfer coefficients (HTC) also increase, which suggests the effect of convective boiling. It is likely that the bubbles emerging from the surfaces of pin fins quickly form vapor core apart from the pin fin surfaces, while a thin liquid film is located

on the pin fin surfaces. This flow pattern corresponds to intermittent and annular flow patterns. In terms of heat transfer coefficient (HTC), Configuration #1 has the lowest performance when compared with other plates. Configuration #2 and Configuration #3 exhibit almost the same HTC, and their heat transfer enhancement is almost the same when they are compared with reference plate (Configuration #1), especially at high mass flux. The difference in the heat transfer coefficient (HTC) between Configuration #4 and Configuration #5 increases with the mass flux. Thus, there exists a significant enhancement in heat transfer with the use distribution of pin fins with no tip clearance and elliptical pin fins along the heating region (Configuration #5). Obtained results prove that the distribution pin fin area significantly affects the heat transfer performance (when comparing Configuration #2 with Configuration #4). In other words, these circular pin fins are able to provide a more homogenous flow distribution along the heat sink, and it becomes unlikely that vapor growing due to phase change migrates towards the inlet, which is reflected as a better performance. However, in this study, there are not positive effects of tip clearance. Moores and Joshi [43] presented the tip clearance effects and they reported that there was a significant effect of tip clearance when it was at most 10% lower than exact pin fin height. They reported that low tip clearance levels can induce accelerated flow and reduce the development of recirculating of bubbles. The same trends can be observed in this study. Configuration #3 (with higher tip clearance) presents intense bubble recirculation while Configuration #5 (without tip clearance) delays larger bubble coalescence due to the accelerated flow and result in heat transfer enhancement. Moreover, larger tip clearance leads to a reduction in flow rates within the arrays and results in a lower heat transfer enhancement while smaller tip clearances offer a high heat transfer performance due to additional surface area. Therefore, no enhancement is observed in this study with the use of tip clearance (for Configuration #3 and
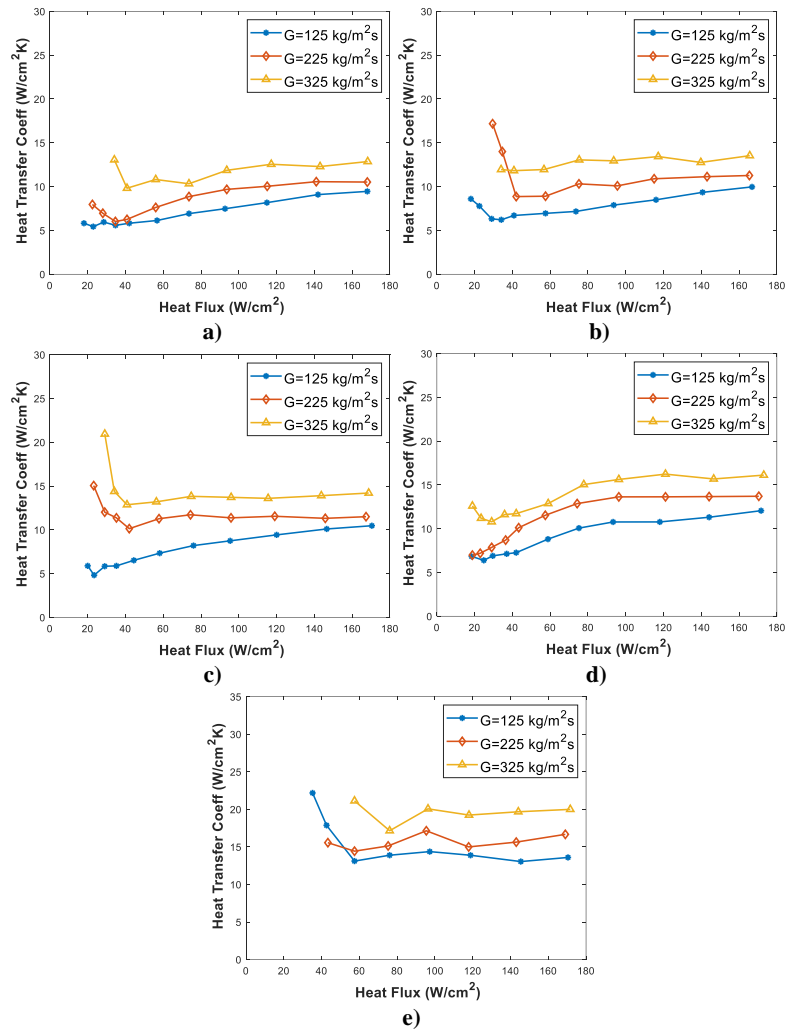
Configuration #4).

Figure 11 Heat transfer coefficients profiles for each mass flux a) Configuration #1, b) Configuration #2, c) Configuration #3, d) Configuration #4, and e) Configuration #5.

In addition to the average heat transfer coefficient profiles, local heat transfer coefficient profiles are also presented in as a function of local quality Figure 12 along the channel to complement the boiling heat transfer data.
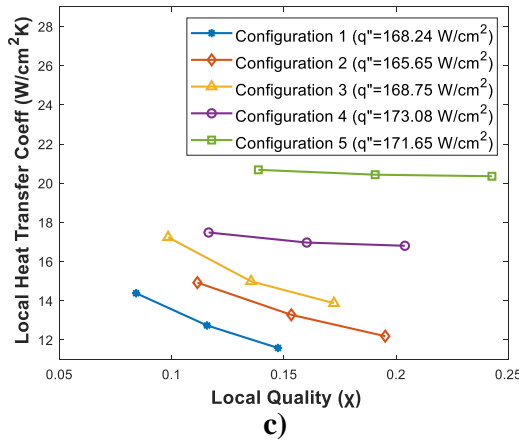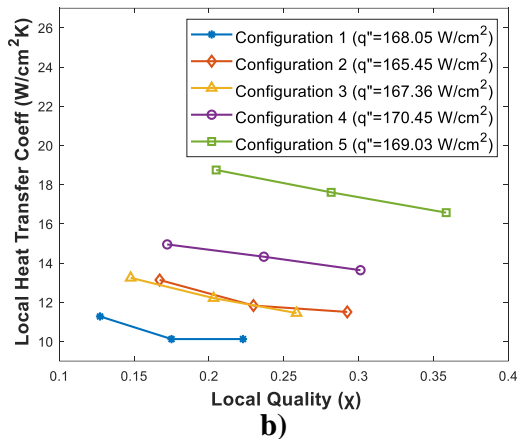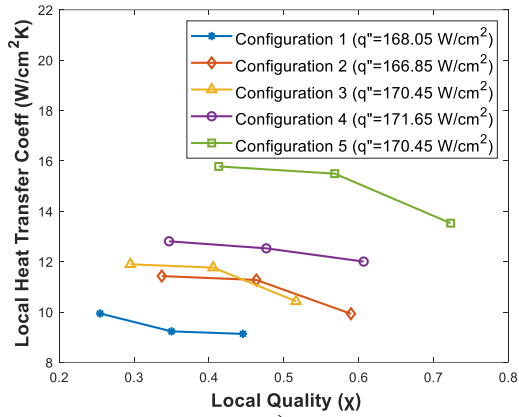
Figure 12 Variation of local heat transfer coefficient as a function of location a) G = 125 kg/m^{2}s, b) G = 225 kg/m^{2}s, c) G = 325 kg/m^{2}s at high heat flux ($q'' > 165 \, W/cm^2$).

Boiling images for each plate are presented in Figure 13 and Figure 14. The flow direction is shown in both figures from left to right. Bubbly flow (at low heat flux), intermittent (low – medium heat flux) and annular (high heat flux) flow patterns can be detected. Nucleate boiling is associated with bubbly flow pattern, while annular flow pattern

corresponds to convective boiling. It can be also visually observed that bubbly flow regime is seen at low heat fluxes particularly near the inlet, while annular flow regime can be recognized at higher heat flux particularly near the outlet. In addition, annular flow occurs earlier in Configuration #1 compared to other configurations. It can be also concluded that the formation of intermittent and annular flow regime is observed for Configuration #1 at the lowest mass flux ($G = 125 \, kg/m^2 s$), and nearly dry-out condition is reached at the highest heat flux ($q'' > 165 \, W.cm^{-2}$). Moreover, nucleated bubbles are observed at the inlet region of Configuration #1. On the other hand, there is a slight difference between Configuration #2 and Configuration #3 regarding boiling images. As the heat flux increases, the elongated bubbles are observed on the elliptical pin finned area at the outlet region of the channel, and large vapor core can be seen at low mass flux. Moreover, it can be observed that the existence of an elliptical pin finned area between the channels also affects the bubble coalescence. In addition, intermittent flow and annular flow regimes are mainly observed within a wide range of heat flux at lower mass flux. Bubble formation is observed at the stagnation points of the pin fins, and these bubbles depart by rising above the pin fins with the flow due to the tip clearances (for Configuration #3 and Configuration #4). Furthermore, bubbles coalescence on the surface of pin fins and on the surface of the channel occurs, thereby leading to vapor slugs. For the configurations with tip clearance (Configurations #2 and #3), there is less improvement in heat transfer due to significant vapor core formation, where the bubbles coalesce and occupy entire cross section and move to outlet region on the presence of tip clearance. Additionally, Configuration #4 (with the same tip clearance as Configuration #2 but with distribution pin fins) has a better performance. The distribution pin fins provide an enhancement in heat transfer due to homogenous flow distribution effect on the channel as well as blockage for vapor towards the inlet. Elongated bubble form on the elliptical pin finned area and bubble coalescence take place at a nearer location to the outlet of the channel at a higher mass flux.
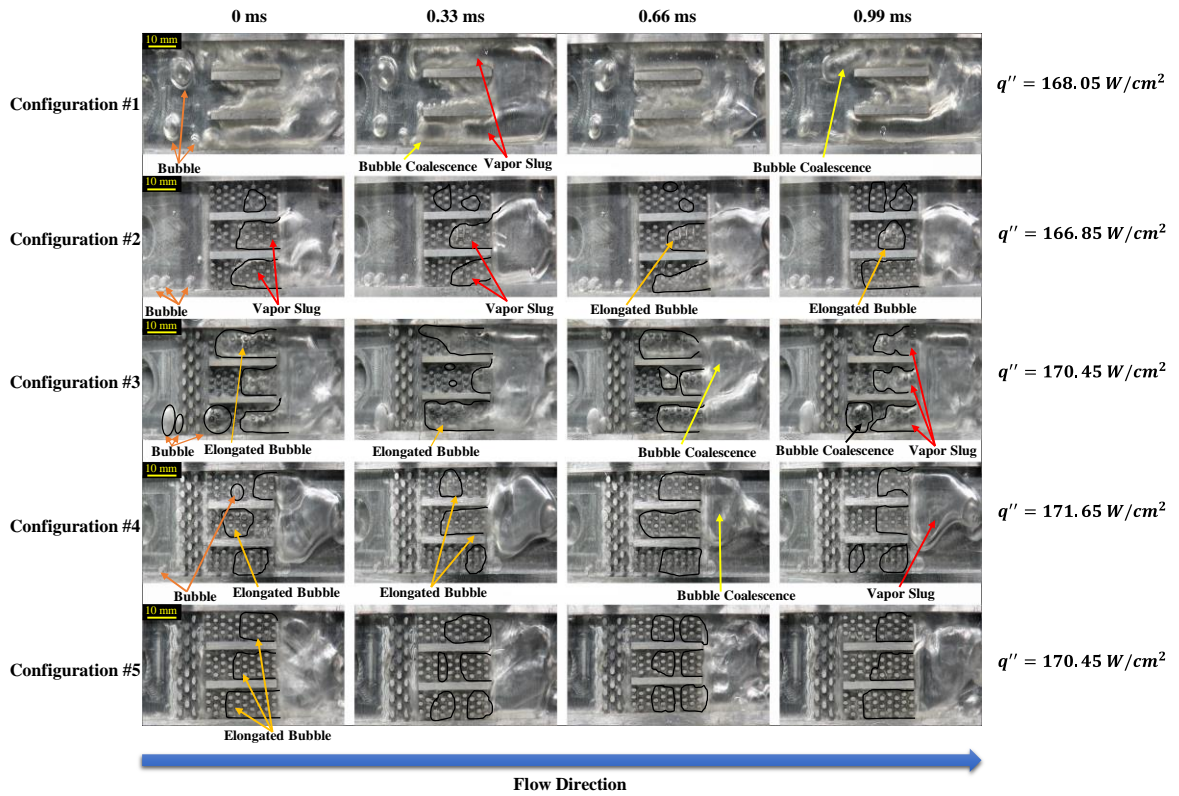
Figure 13 Boiling images at lowest mass flux (G = 125 kg/m^{2}s) and high heat flux ($q'' > 165\ W.cm^{-2}$) for each configuration.

At higher mass fluxes, bubbly flow is observed for each heat sink near the inlet region, and nucleate boiling could be dominant even at high heat flux. While bubbly to annular flow regime is observed at the lowest mass flux, mostly bubbly flow and intermittent flow regimes could be detected at the highest mass flux in Configurations #3-5. It can be also recognized that the transitions from bubbly to intermittent flow (or elongated bubble) patterns and intermittent-annular flow patterns are delayed with pin fins.
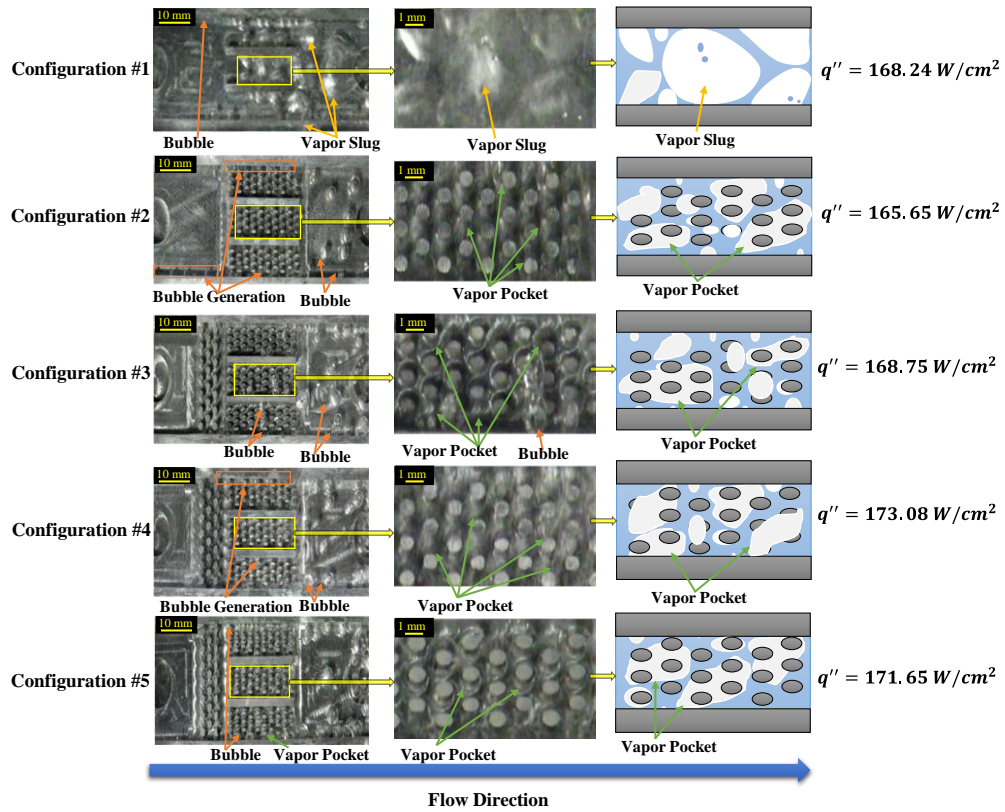
Figure 14 Boiling images at highest mass (G = 325 kg/m²s) and high heat flux ($q'' >$ $165\ W.cm^{-2}$) for each configuration.

To provide a flow pattern map, each configuration is divided into 10 locations based on visual images at mass flux ($G = 125\ kg/m^2 s$), which provide relative transition between the flow regimes (Figure 15). Accordingly, the flow pattern map is divided into four regions: single-phase flow (SP), bubble flow (BF), intermittent flow (IF), and annular flow. Boiling number, which is a major nondimensional parameter in flow boiling and is expressed as: $Bo = q''_w/Gh_{fg}$, is employed in similar lines with the literature [77,78]. Single-phase flow is mainly observed at inlet region at lower heat fluxes and does not include any formation of vapor phase. Vapor formation starts with isolated bubbles observed at nearer location on the elliptical pin finned area. The diameter of these bubbles is relatively smaller than major dimensions of elliptical pin fins so that no bubble coalescence could be observed. However, intense bubble coalescence and growth could be detected along the longitudinal direction as well as with heat flux. As a result, intermittent flow could be detected, which includes intense bubble coalescence and resulting formation of elongated slug. Further increase in heat flux results in the formation

28

of annular flow regime. The absence of pin fins causes early transition among the flow regimes (Configuration #1). Annular flow regime could be detected at moderate heat fluxes for Configuration #1. However, the presence of pin fins delays annular flow regime even at high heat fluxes. The combination of elliptical pin fins with distribution pin fins promotes the delay in flow pattern transition (Configuration #5). Similar trends could be observed at other mass fluxes (Figure 16 and Figure 17). It can be seen that flow patterns shift to a more upstream location with heat flux for each map. In addition, the flow pattern transitions shift towards the outlet with increasing mass flux so that the annular flow pattern cannot be detected under certain conditions (high mass flux, pin fin configuration).
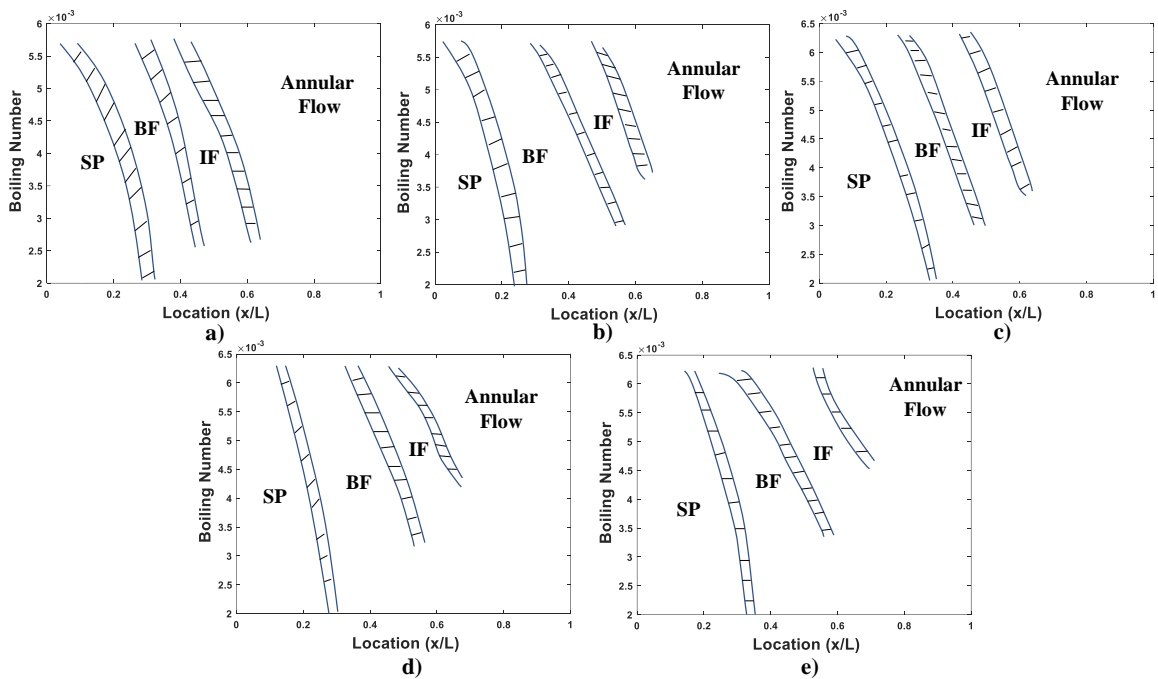
Figure 15 Flow regime map at lowest mass flux (G = 125 kg/m^{2}s) a) Configuration #1, b) Configuration #2, c) Configuration #3, d) Configuration #4 , and e) Configuration #5.
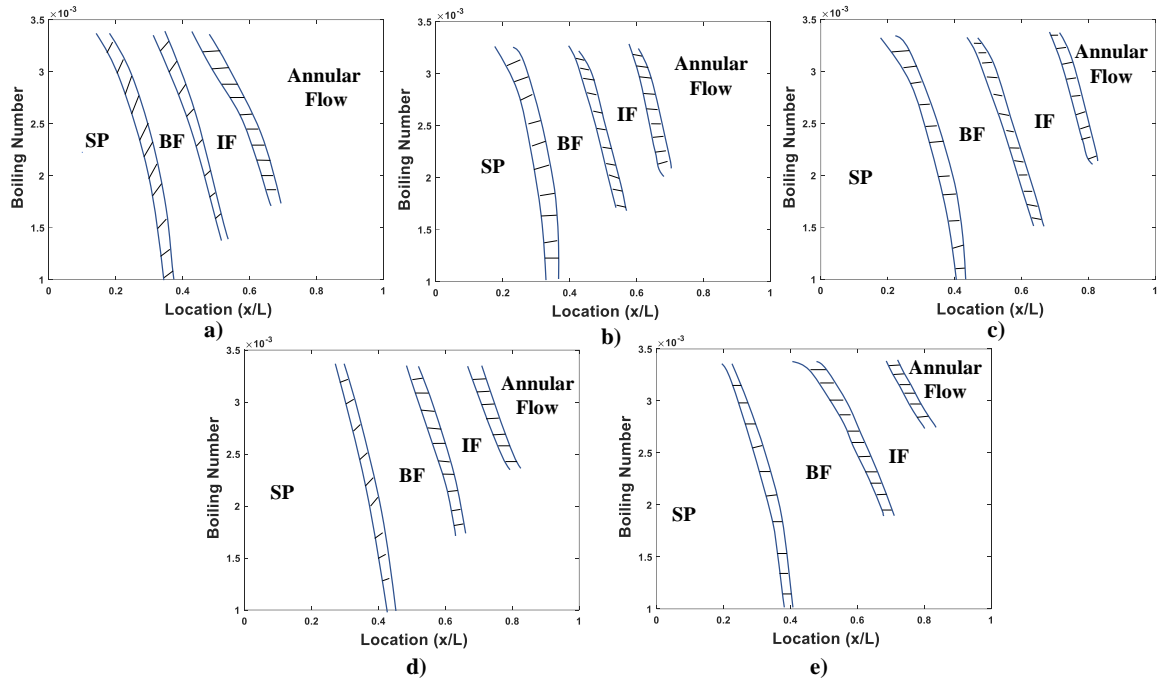
Figure 16 Flow regime map at medium mass flux (G = 225 kg/m^{2}s) a) Configuration #1, b) Configuration #2, c) Configuration #3, d) Configuration #4, and e) Configuration #5.
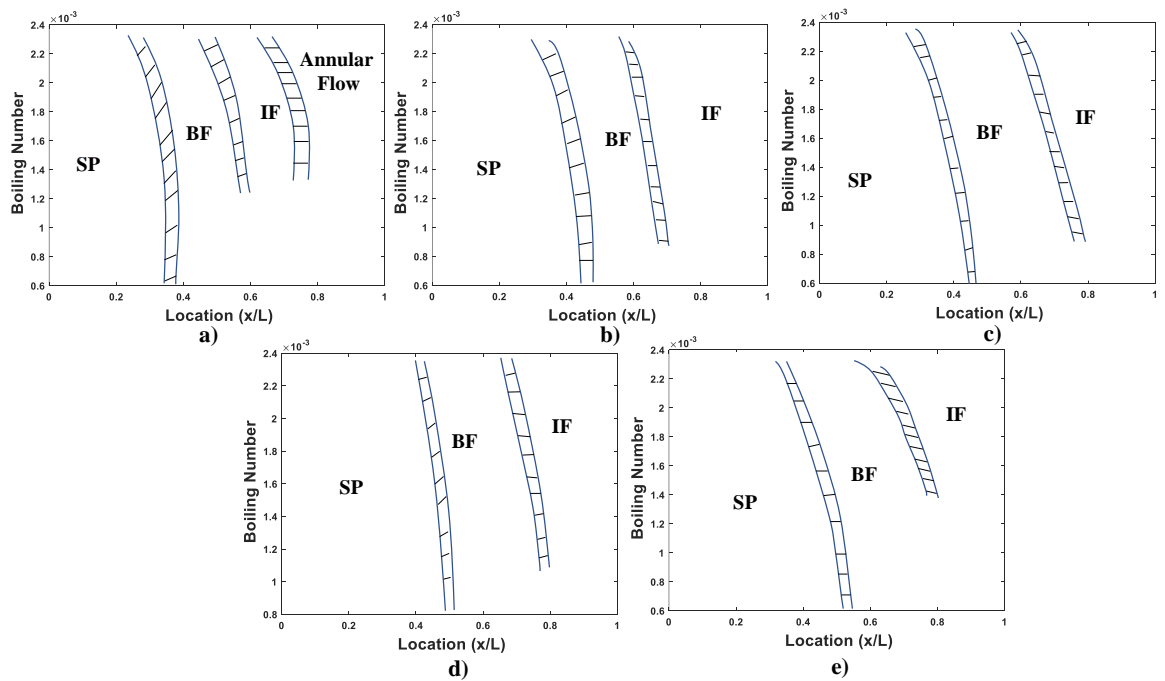
Figure 17 Flow regime map at highest mass flux (G = 325 kg/m^{2}s) a) Configuration #1, b) Configuration #2, c) Configuration #3, d) Configuration #4, and e) Configuration #5.

3. CHAPTER 3: POOL BOILING HEAT TRANSFER ON MODIFIED (superhydrophilic, superhydrophobic, and superbiphilic) SURFACES

3.1. Objectives

The use of biphilic surfaces is very promising approach to enhance heat transfer at both atmospheric and sub-atmospheric pressures. Although there are number of research efforts available in the literature for atmospheric pressure, there are limited studies available at sub-atmospheric pressure. This study aims to reveal the wettability effect at both atmospheric and sub-atmospheric pressures using four different (homogenous and mixed wettable) surfaces. This study also provides a facile fabrication method to obtain superbiphilic surfaces. Boiling and HTC curves, and as well as visualization results are presented for different pressures and surfaces to reveal the wettability effect.

3.2. Experimental Methods

3.2.1. Surface functionalization and modification

In this section, the fabrication process of samples with different wettability features is explained. Samples were made of aluminum alloys (composition: Al 92.9%, O 3.7%, C 2.8%, Mg 0.4%, Si 0.1%) – 1050 with a diameter of 50.8 mm and a thickness of 2 mm were used to fabricate functional surfaces. Four samples were modified to achieve superhydrophilic (Sample #1), superhydrophobic (Sample #2), and superbiphilic (Sample #3 and #4) surfaces. Hydrochloric acid (37%, Merck), Stearic Acid (99%, Lancaster), Ethanol (99%, Merck), Acetone (99%, Merck), and deionized water were used during the fabrication. The fabrication of the superhydrophilic surface has 2 steps: the wet etching process and laser texturing. The superhydrophobic surfaces were fabricated through 3 steps: wet etching process, laser texturing, and acid functionalization. In the fabrication of the superbiphilic surfaces, there are also 3 steps: wet etching process, acid

functionalization, and laser texturing. The schematics of fabrication processes are presented in Figure 18.
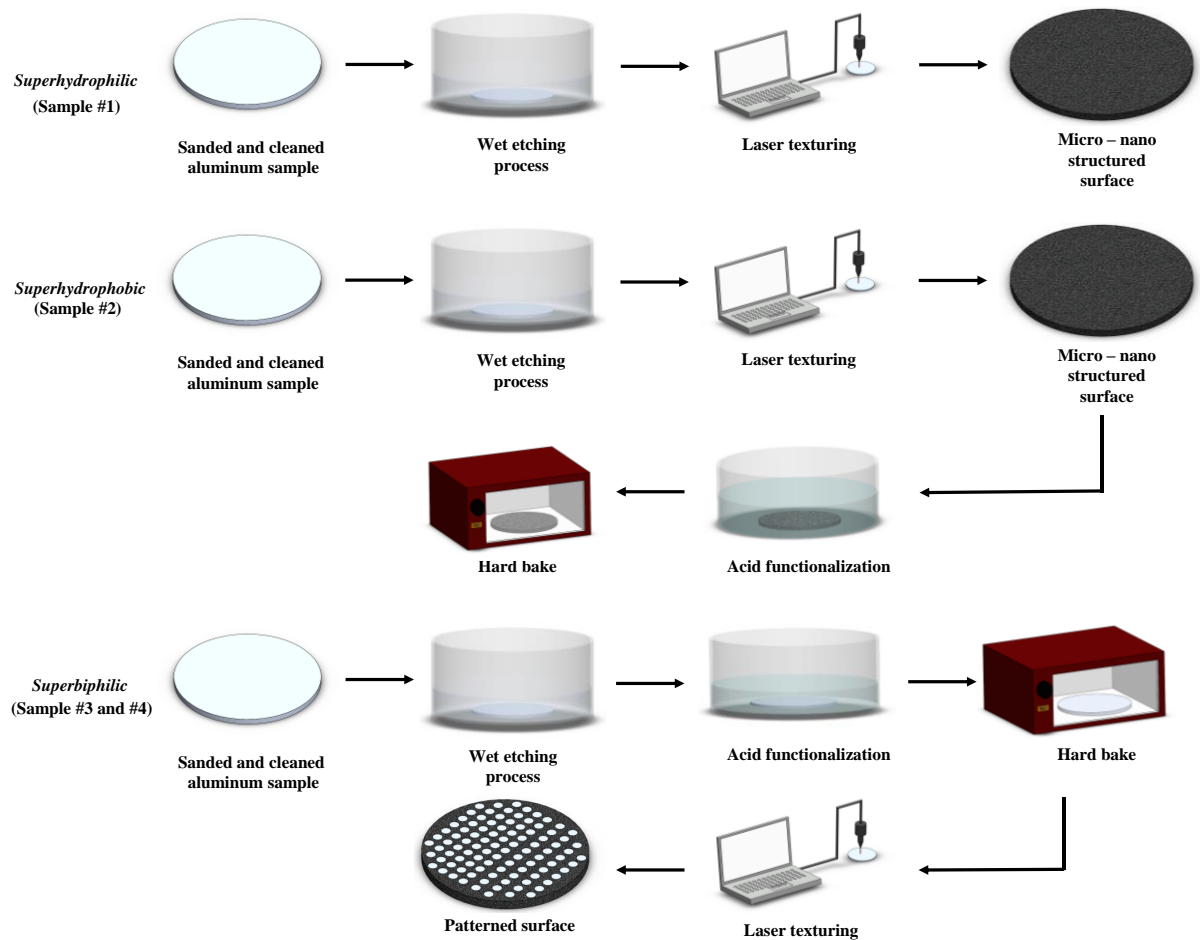
Figure 18 Schematics of fabrication processes of superhydrophilic (Sample #1), superhydrophobic (Sample #2), and superbiphilic (Samples #3 and #4) surfaces.

All the aluminum samples were first rinsed with deionized water. Then, aluminum samples were sanded with P400, P600, P800, P1000, P1200, and P2000 sandpapers using the polishing machine (METKON - Gripo 2V) to obtain mirror-like surfaces with a roughness of approximately $S_a = 0.15\ \mu m$. Thereafter, the samples were washed with deionized water several times and were dried with a nitrogen gun, and immersed at an ultrasonic bath temperature of $60^{\circ}C$ by using deionized water and acetone mixture ($V_{acetone}:V_{deionized\ water}$: 1/5:1) for 10 minutes. Then, the samples were washed with deionized water several times to ensure that the residuals of acetone were fully cleaned from the surfaces and were dried with a nitrogen gun. For the etching process, the solution was prepared as a mixture of HCl (hydrochloric acid) and deionized water with a volume ratio of 1:1, and each sample was immersed for 3-4 minutes. The samples were again

washed then with deionized water several times, were immersed in a mixture of acetone and deionized water using an ultrasonic bath for 10 minutes, and were washed with deionized water several times to ensure that the ruins of acetone and hydrochloric acid (HCl) were fully cleaned and were dried with a nitrogen gun.

3.2.1.1. *Superhydrophilic (Sample #1) and superhydrophobic surface preparation*

After the etching process, laser texturing was performed on the samples (#1 and #2) to obtain superhydrophilicity with a CA~0°. Moreover, this process also provided a more hydrophobic area with the formation of microstructures owing to the surface after acid functionalization (Sample #2).

Table 3 Description of wettability and surface characteristics of each sample.

Sample Number	Static contact angle of the hydrophobic region (CA)	Static contact angle of the hydrophilic region (CA)	Superhydrophobicity ($A^* = A_{SHP}/A_{Total}$)	Pitch size (mm)	Spot diameter (mm)
Sample #1	-	~0°	-	-	-
Sample #2	158	-	100%	-	-
Sample #3	155	~0°	11.30%	5	0.7
Sample #4	154	~0°	28.31%	3	0.7

For acid functionalization, the solution was prepared with 20 ml of ethanol and 15 mM stearic acid to obtain superhydrophobicity for Samples #2, #3, and #4. For this step, closed containers were used to mix stearic acid and ethanol solution. The stearic acid mixture was shaken and kept in the oven for 15 minutes at 60°C to obtain a homogenous solution. Then, the samples were placed in a cleaned container, and the homogeneous solution was spilled on the samples for 120 minutes to obtain a superhydrophobic surface. After this process, the samples were dried in the oven for 6 hours at 120°C and were left to cool down at room temperature. At the end of this process, superhydrophobic surfaces were obtained. The contact angle results are presented in Table 3. Optimization was made

to have the optimum time since longer or shorter waiting times might lead to deviations from the desired contact angles.

3.2.1.2. *Fabrication of superbiphilic surfaces*

To fabricate superbiphilic surfaces, at first superhydrophobic surfaces (background) were prepared using acid functionalization. Next, laser texturing was implemented to provide areas with the WCA<1° [80]. For this, at first, the patterns were designed via Computer-Aided Design (CAD) software. Next, FLAST (FiberLAST) marking system was used to remove the desired superhydrophobic regions (outside of spots) and form superhydrophilic regions via laser (Figure 19). The laser texturing provided an enhanced spot shape for superhydrophobic regions since direct exposure could be applied to the surfaces from the CAD file. Thus, the desired shape and dimensions of the superhydrophobic region on the surface could be obtained with ablation and melting of the surface.
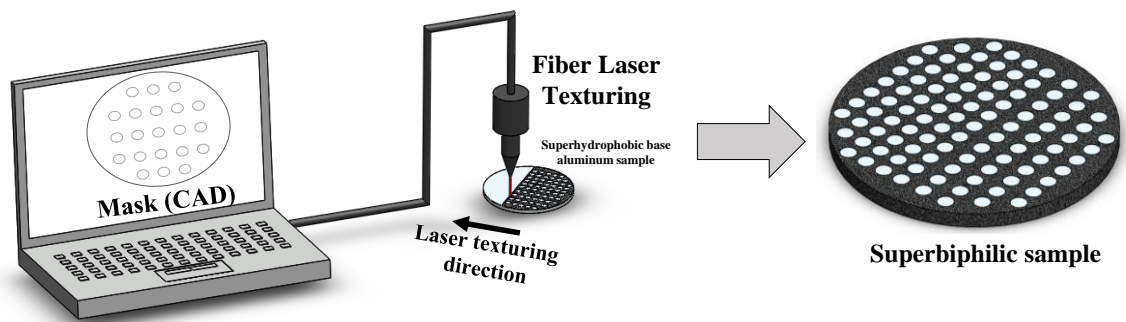
Figure 19 The scheme of the laser texturing process to obtain mixed wettability (superbiphilic) surface.

Laser texturing was applied at an average power of 10 W, scanning velocity of 250 mm.s^{-1}, pulse frequency of 100 kHz, a wavelength of λ=1064 nm, and the beam spot diameter of 40 μm with a parallel laser beam. The samples were textured at open-air and ambient temperatures. Preliminary laser texturing tests were carried out to ensure that the superhydrophilic region was obtained with minimal damage on the surface and maximum achievement on CA ($\sim$0°). The corresponding spots were designed in such a way that the spot diameter of 0.7 mm for both surfaces, and pitch sizes of 3 mm and 5 mm for Samples #3 and #4 were formed, respectively. An overview of the fabricated superbiphilic surfaces is presented in Figure 20. Moreover, the same laser texturing process was implemented

to the etched surfaces (Sample #1 and #2) to obtain an entirely superhydrophilic region and the same microstructured region. To obtain the zoom-in images of fabricated surfaces Samples #3 and #4, a 'Zeiss Stemi DV4 Stereo Microscope' was used (Figure 20).
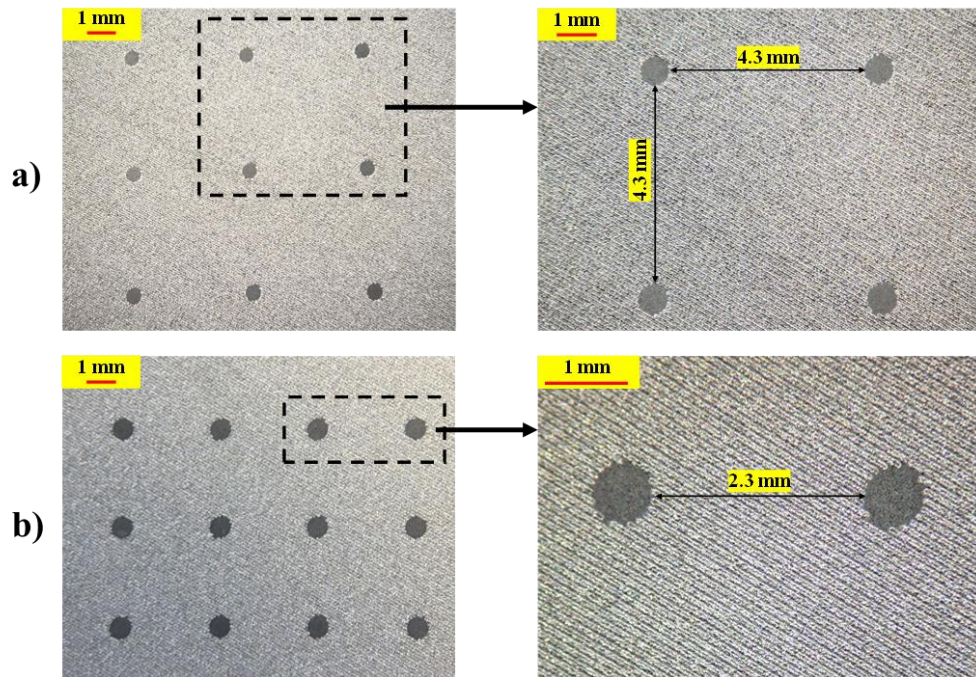
Figure 20 Configurations of fabricated samples a) Sample #3 (diameter of 0.7 mm and pitch size of 5 mm) b) Sample #4 (diameter of 0.7 mm and pitch size of 3 mm).

3.2.2. Surface Characterization

An Attention Theta Lite optical tensiometer system was used to measure the contact angle of the samples. For this purpose, the static contact angle was measured at different locations. Moreover, the average contact angle was recorded by analyzing the captured images. A summary of measurement results is presented for each sample in Table 3. The contact angle measurements were performed with the use of 5μl droplets of deionized water on the surfaces and captured contact angle measurement results are presented in Figure 21. The contact angle measurements were performed after each step of fabrication (sanding, wet etching, acid functionalization, and laser texturing) and after the experiments for homogenous superhydrophilic (Sample #1) and superhydrophobic (Sample #2) surfaces. There were insignificant changes regarding the contact angle ($\sim 0^{\circ}$) on the superhydrophilic surface. In addition to the contact angle measurements, Scanning

Electron Microscope (SEM) images were also obtained at an accelerating voltage of 10 V for modified surfaces (superbiphilic) to analyze the surface morphology of superhydrophobic spots and superhydrophilic regions, as presented in Figure 22. The obtained figure proves that laser texturing on the superhydrophobic surface leads to the desired superhydrophobic spots in terms of both the diameter and desired shape.
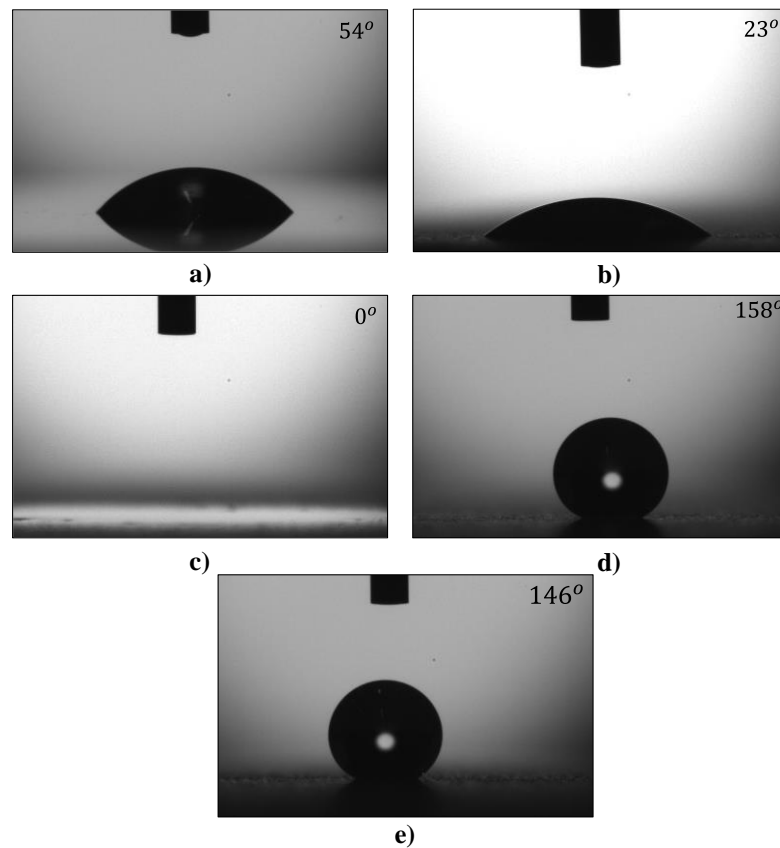
Figure 21 Contact angle measurements a) polished bare aluminum plate, b) etched aluminum plate, c) laser textured aluminum plate (Sample #1), d) functionalized aluminum plate as superhydrophobic surface (Sample #2), and e) homogenous superhydrophobic surface after boiling experiments.
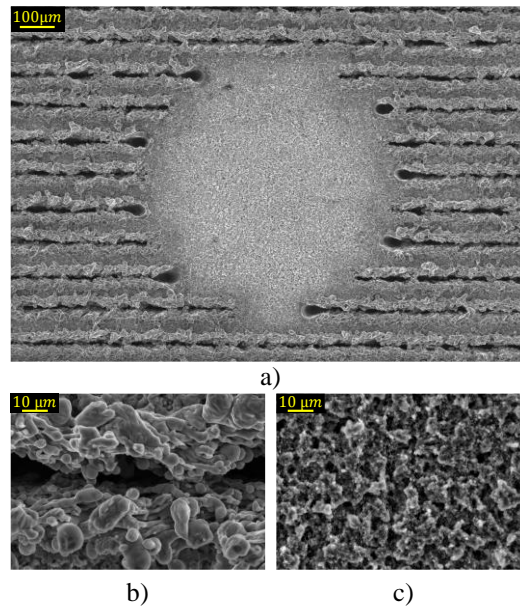
Figure 22 Scanning Electron Microscopy images of Sample #4 (with a pitch size of 3 mm and diameter of 0.7 mm) a) SEM results showing the pattern on the sample, b) laser textured region (superhydrophilic region), c) superhydrophobic spot.

3.2.3. Experimental setup and procedure

The experimental setup used during pool boiling experiments is shown in Figure 23. The main components of the experimental setup include a vacuum pump, condenser, aluminum heater, PTFE block, cartridge heaters, power supply, high speed camera, data acquisition system, and preheaters. The boiling chamber was designed to have dimensions of 200x200x250 mm^3. It was made of aluminum alloy and has transparent windows, which were made of polycarbonate and were located on three sides of the test section to allow visualization. To assemble the boiling chamber, a silicon plaque was used to ensure that there was no leakage. An aluminum block heater was located at the bottom of the test section, and five cartridge heaters of a diameter of 9 mm and a length of 70 mm were placed into the aluminum heater to obtain the desired heat fluxes using a power supply. The sample was placed above the aluminum heater and was sandwiched into a 2 mm thickness of stainless-steel holder. The surface of the aluminum plate and heater were treated with a high-quality thermal paste to reduce the thermal resistance. The outer surface of the aluminum heater was surrounded by PTFE to reduce heat losses. Two preheaters were placed on two sides of the boiling chamber to obtain the constant

37

saturated liquid before starting the experiments. One power supply was connected to the preheaters for this purpose. The condenser was located above the chamber to keep the pressure constant. The vacuum pump was connected to a pressure gauge to fix the pressure at the desired values. A pressure gauge was used to measure and fix the pressure during the experiments. Two thermocouple holes with a diameter of 1 mm were placed on the aluminum heater to obtain the surface temperature data using T-type thermocouples (Figure 24). The high-speed camera (at a frame rate of 3000 s^{-1}) was placed in front of the transparent window to obtain visualization (boiling images) data during pool boiling experiments. Experimental data were acquired by recording the temperature data, heat flux data, and boiling images under steady-state conditions for each sample.
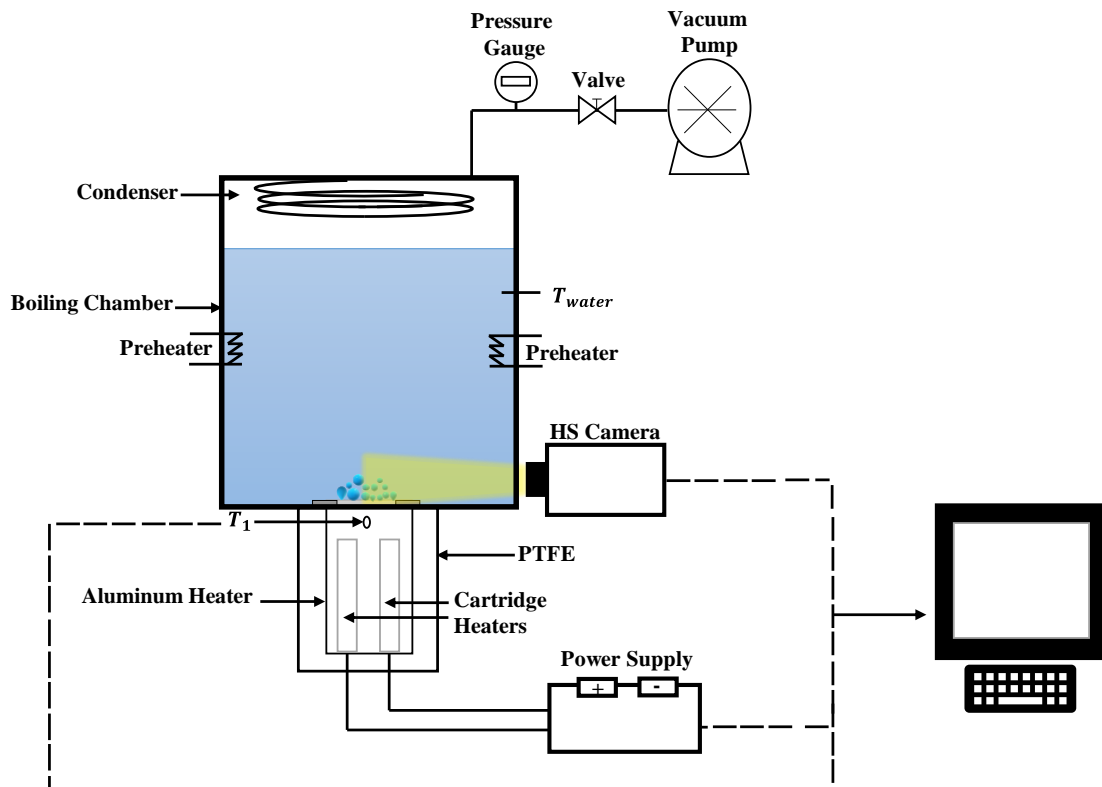
Figure 23 Schematic of the experimental setup for boiling heat transfer tests.

The experiments were conducted at the saturation temperature and atmospheric (103.7 kPa) and sub-atmospheric (28.3 kPa) pressures. Deionized water was used as the working fluid. The boiling chamber was closed with an aluminum cap, which included a condenser, pressure gauge, and connected vacuum pump. For sub-atmospheric tests, the pressure was decreased to the desired sub-atmospheric pressure. Deionized water was heated to the saturation temperature by the preheater before the tests. During the tests, the

38

desired heat flux was applied to the sample, and after having steady-state conditions, all the corresponding data were acquired. This process was repeated for different heat flux values.
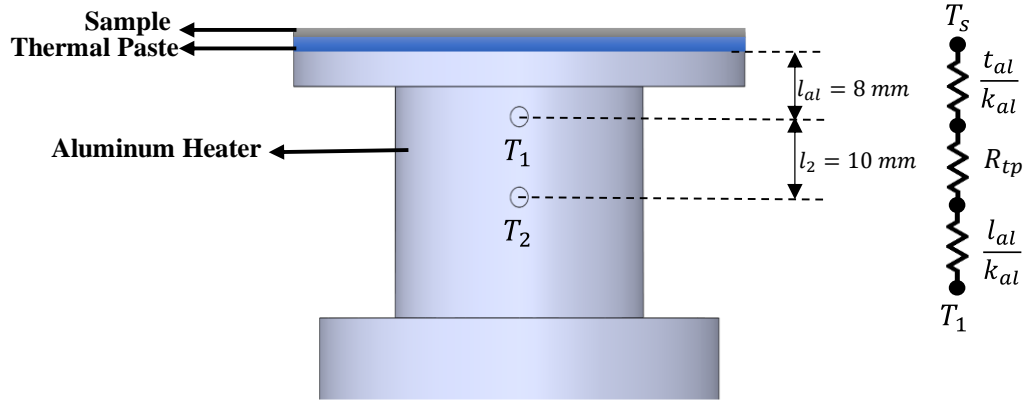
Figure 24 Thermocouple locations for surface temperature measurements.

3.3. Data reduction and data analysis

First, the electrical power is calculated using the voltage and current data as:

$$P = VI \hspace{3cm} (23)$$

where V is the voltage, and I is the current. The aluminum heater has surrounded by a PTFE block to reduce heat losses. Additionally, heat losses were calculated as the difference between input power and the amount of removed heat in the single-phase regime. For each test, natural convection analysis was performed to calculate the heat losses. Heat losses were found to be less than 15% for each test. The net heat flux is calculated as:

$$q'' = \frac{VI - Q_{loss}}{A} \hspace{3cm} (24)$$

where Q_{loss} is the heat loss and A is the heated surface area. The surface temperature (T_s) can be found according to 1- D heat conduction analysis as:

$$T_s = T_1 - q'' \left(\frac{l_{al}}{k_{al}} + R_{tp} + \frac{t_{al}}{k_{al}} \right) \hspace{2cm} (25)$$

where T_1 is the temperature on the exact location of the aluminum heater, $R_{tp} = 6x10^{-6} (\frac{m^2 K}{W})$ is the thermal resistance of the thermal paste, l_{al} is the distance between the T_1 and aluminum heater surface, and t_{al} is the thickness of the aluminum samples. Moreover, to obtain the exact pressure at the surface, the head pressure is also considered

for calculating the liquid pressure as:

$$P_{sat} = P_s + \rho_f gH \qquad (26)$$

where P_s is the system pressure, ρ_f is the fluid density at exact pressure, g is the gravitational constant, and H is the height of the liquid inside the boiling chamber. Finally, the heat transfer coefficient is calculated as:

$$h = \frac{q''}{T_s - T_{sat}} \qquad (27)$$

where T_s is the surface temperature of the sample and T_{sat} is the saturation temperature at the exact pressure of deionized water. An uncertainty analysis was performed based on the uncertainty propagation method [73]. Accordingly, the uncertainty in an experimental parameter is expressed as:

$$U_y = \sqrt{\sum_{i=1}^{n}\left\{\left(\frac{\partial y}{\partial a_i}\right)\cdot U_{a_i}\right\}^2} \qquad (28)$$

where U_{a_i} is the uncertainty in the parameter a_i. The uncertainties in this study are presented in Table 4. They were either provided by the manufacturers or were calculated using the uncertainty propagation method [73].

Table 4 Estimated uncertainties in experimental parameters.

Parameters	Uncertainty
Voltage	± 1 V
Current	± 0.01 A
Wall Temperature	± 0.3 K
Fluid Temperature	± 0.3 K
Heat Transfer Coefficient (HTC)	$\pm 5 - 7\ \%$
Pressure	$\pm 0.25\ \%$

3.4. Validation

To validate the experimental results, a polished bare aluminum plate was used. The results were compared with the predictions of the Rohsenow correlation [81], which is widely utilized in pool boiling heat transfer, and is expressed as:

$$q'' = \mu_l h_{fg}\left[\frac{g(\rho_l - \rho_v)}{\sigma}\right]^{0.5}\left[\frac{c_p \Delta T}{C_{sf}h_{fg}Pr^n}\right]^3 \qquad (29)$$

where h_{fg} is the latent heat of working fluid, ρ_v is the density of vapor phase of the working fluid, ρ_l is the density of liquid phase of the working fluid, σ is the surface tension, C_{sf} is surface constant, g is gravitational constant, Pr is Prandtl number, c_p is the specific heat, and ΔT is the wall superheat, which is the difference between the surface temperature and saturation temperature of the working fluid.

The comparison between the predictions of the Rohsenow correlation and experimental results is displayed in Figure 25. As can be seen, the experimental results closely match the predictions of the correlation (with a maximum error of 7%).
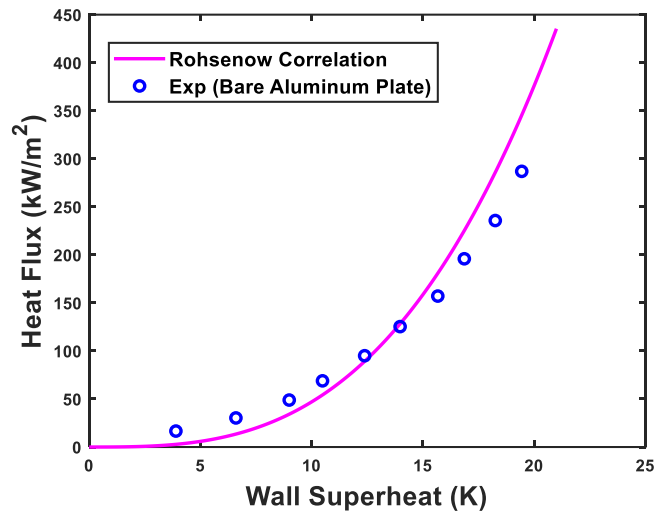
Figure 25 Comparison between the experimental data and predictions of the Rohsenow correlation [81].

3.5. Results and Discussion

Boiling heat transfer results are included in this section to display boiling characteristics for different functional surfaces: superhydrophilic (Sample #1), superhydrophobic (Sample #2), and superbiphilic (Samples #3 and #4) surfaces at atmospheric (103.7 kPa) and sub-atmospheric (28.3 kPa) pressures. Sample #3 has 69 superhydrophobic spots with a diameter of 0.7 mm and a pitch size of 5 mm while Sample #4 has 185 superhydrophobic spots with a diameter of 0.7 mm and a pitch size of 3 mm.

3.5.1. Boiling heat transfer at atmospheric pressure

Figure 26 shows the obtained boiling curves and boiling heat transfer coefficients (HTCs) for tested samples at atmospheric pressure (p=103.7 kPa). Due to the early boiling inception, the homogenous superhydrophobic surface (Sample #2) has a higher heat transfer coefficient compared to the homogenous superhydrophilic surface (Sample #1). The boiling inception starts at lower wall heat fluxes and a higher number of nucleation sites are activated on the superhydrophobic surface (Figure 27a). On the other hand, Sample #1 shows a delay in ONB until a larger wall superheat (ΔT_{sat}=2-3 K) (Figure 26a), resulting in a lower boiling heat transfer, which indicates the enhancing effect of low wettability (CA>150º) on boiling heat transfer. While superbiphilic and superhydrophobic surfaces share the same nature in terms of low surface energy areas, the higher heat transfer coefficients on superbiphilic samples are mainly due to the dynamics of growing and departing bubbles at low/medium heat fluxes. Furthermore, vapor residual on superhydrophobic spots of superbiphilic surfaces [53] and the thermal interaction between randomly distributed nucleation sites [10] at the superhydrophobic surface may be reasons for the lower heat transfer coefficient on Sample#2 compared to superbiphilic surfaces under atmospheric conditions.
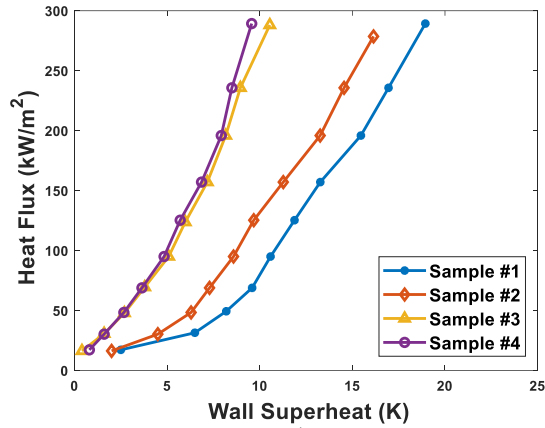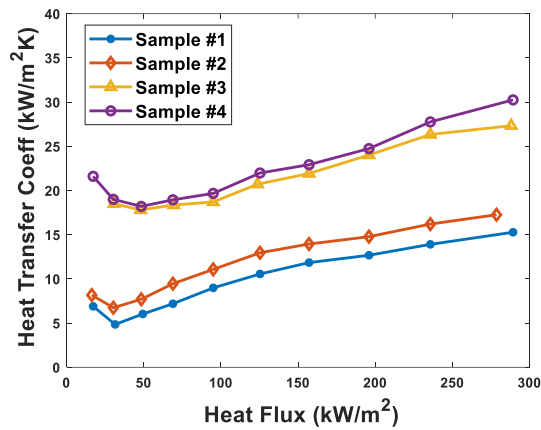
Figure 26 a) Boiling and b) HTC curves for homogenous superhydrophilic surface (Sample #1), homogenous superhydrophobic surface (Sample #2), superbiphilic surface with a spot diameter of 0.7 mm and pitch size of 5 mm (Sample #3), superbiphilic surface with a spot diameter of 0.7 mm and pitch size of 3 mm (Sample #4) at atmospheric (103.7 kPa) pressure.

With a further increase in wall heat flux, isolated bubbles are observed on the homogenous superhydrophobic surface (Sample #2) and superhydrophobic spots on superbiphilic surfaces. Due to the lateral coalescence of departing bubbles with adjacent bubbles, an incremental increase in bubble departure diameter is observed with wall heat flux (Figure 27). The bubble departure diameter for Sample #2 is higher than that of the homogenous superhydrophilic surface (Sample #1), which was also reported by Betz et al. [51]. Due to a large number of activated nucleation sites and their random distribution on the homogenous superhydrophobic surface, more coalesced bubbles can be observed on this surface compared to the superbiphilic samples at atmospheric pressure. The higher

active nucleation site density results in higher heat transfer enhancement on the superbiphilic surfaces compared to the superhydrophilic surface (Sample #1). Nucleated bubbles are visible on the superhydrophobic spots on the superbiphilic surfaces (Figure 27). Furthermore, the bubble interface necking phenomenon (vapor residual after bubble departure) can be detected on these spots. Due to the pinning force on the superhydrophobic regions, intense bubble departure and nucleation co-exist on the superhydrophobic spots of Samples #3 and #4. Furthermore, a surface tension gradient increases the chance of bubble nucleation on the contact line between the superhydrophobic and superhydrophilic regions on the superbiphilic (Samples #3 and #4) surfaces. During the bubble growth period, the buoyancy force acts as the main lifting force while the surface tension force opposes it. Under the experimental conditions, the pitch size (3mm vs. 5mm) has a negligible effect on boiling HTC (Figure 26b). Similar observations have been reported in the literature [82].

Figure 27 Boiling images corresponding to the homogenous superhydrophilic surface (Sample #1), homogenous superhydrophobic surface (Sample #2), superbiphilic surface with a diameter of 0.7 mm and pitch size of 5 mm (Sample #3), superbiphilic surface with a diameter of 0.7 mm and pitch size of 3 mm (Sample #4) at atmospheric pressure (103.7 kPa) a) low heat flux, b) moderate heat flux, and c) high heat flux.

3.5.2. *Boiling heat transfer at sub-atmospheric pressure*

The boiling curves and boiling HTCs of tested samples at sub-atmospheric pressure (p =28.3 kPa) are shown in Figure 28. Boiling inception is first detected on the homogenous superhydrophobic (Sample #2) surface and superhydrophobic spots on Samples #3 and #4. The homogenous superhydrophobic surface has a better performance than the homogenous superhydophilic surface due to the early onset of nucleate boiling and the higher number of activated nucleation sites. At low heat fluxes, the mixed wettability surfaces (Samples #3 and #4) exhibit significant heat transfer enhancement compared to the homogenous superhydrophilic (Sample #1) and superhydrophobic (Sample #2) surfaces. Since the number of active nucleation sites considerably decreases with the system pressure, the designated nucleation sites at very low wall heat flux (7.1 kW/m^2) are more effective at sub-atmospheric pressure compared to the atmospheric condition. At moderate heat fluxes, superbiphilic surfaces are superior to the homogenous superhydrophilic (Sample #1) and homogenous superhydrophobic (Sample #2) surfaces. The results are also in good agreement with the literature [61]. At high heat fluxes, the best performance can be still achieved with the superbiphilic (Samples #3 and #4) surfaces.
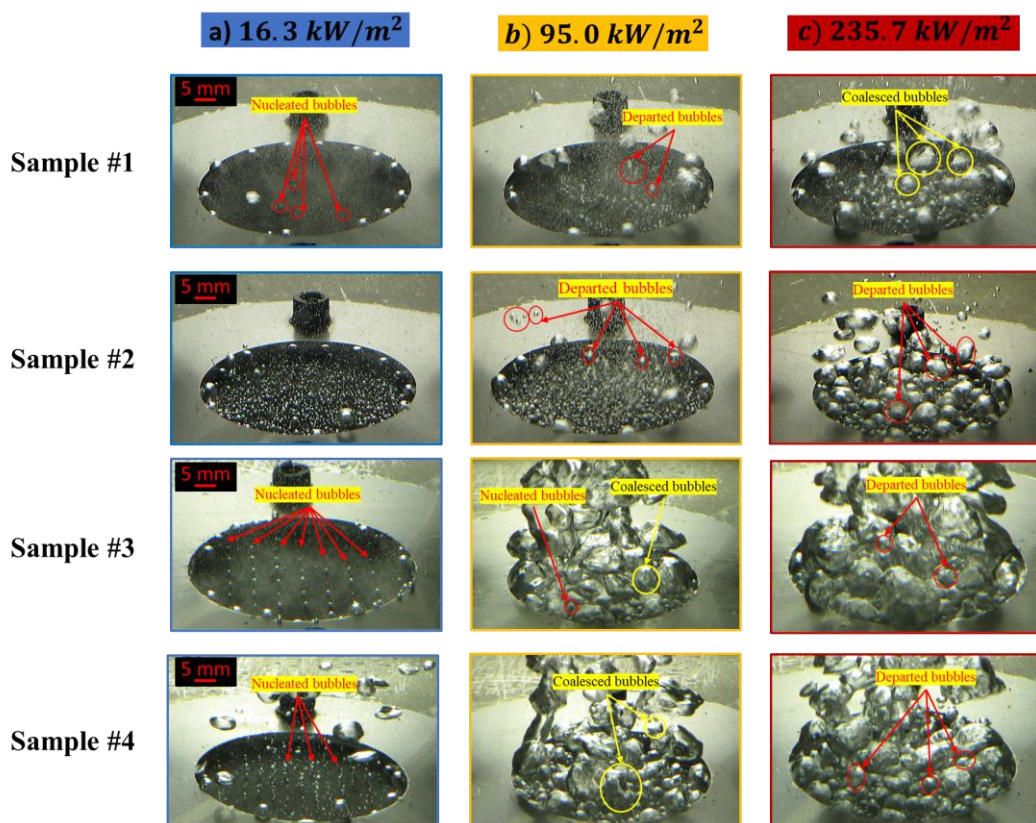
Figure 28 a) Boiling curves and b) HTC curves for homogenous superhydrophilic surface (Sample #1), homogenous superhydrophobic surface (Sample #2), superbiphilic surface with a diameter of 0.7 mm and pitch size of 5 mm (Sample #3), and superbiphilic surface with a diameter of 0.7 mm and pitch size of 3 mm (Sample #4) at sub-atmospheric (28.3 kPa) pressure.

Sample #4 (superbiphilic surface with 3 mm pitch size) performs better than Sample #3 (superbiphilic surface with 5 mm pitch size) due to the higher number of active nucleation sites (185 vs. 69, respectively). The schematic pictures of bubble behavior on superbiphilic surfaces with different pitch sizes at various pressures are shown in Figure 29. Since the low heat flux condition is mainly addressing the bubble nucleation and growth period, the pitch size has a negligible effect on BHT in this region. As the heat flux increases, the role of bubble coalescence and departure on boiling heat transfer becomes more evident. At the developed nucleate boiling region (moderate wall heat fluxes), Sample #4 with a higher nucleation site density and lower pitch size leads to higher boiling HTCs. The lower pitch size contributes to boiling heat transfer by increasing the coalescence induced bubble departure at sub-atmospheric pressure (Figure 29).
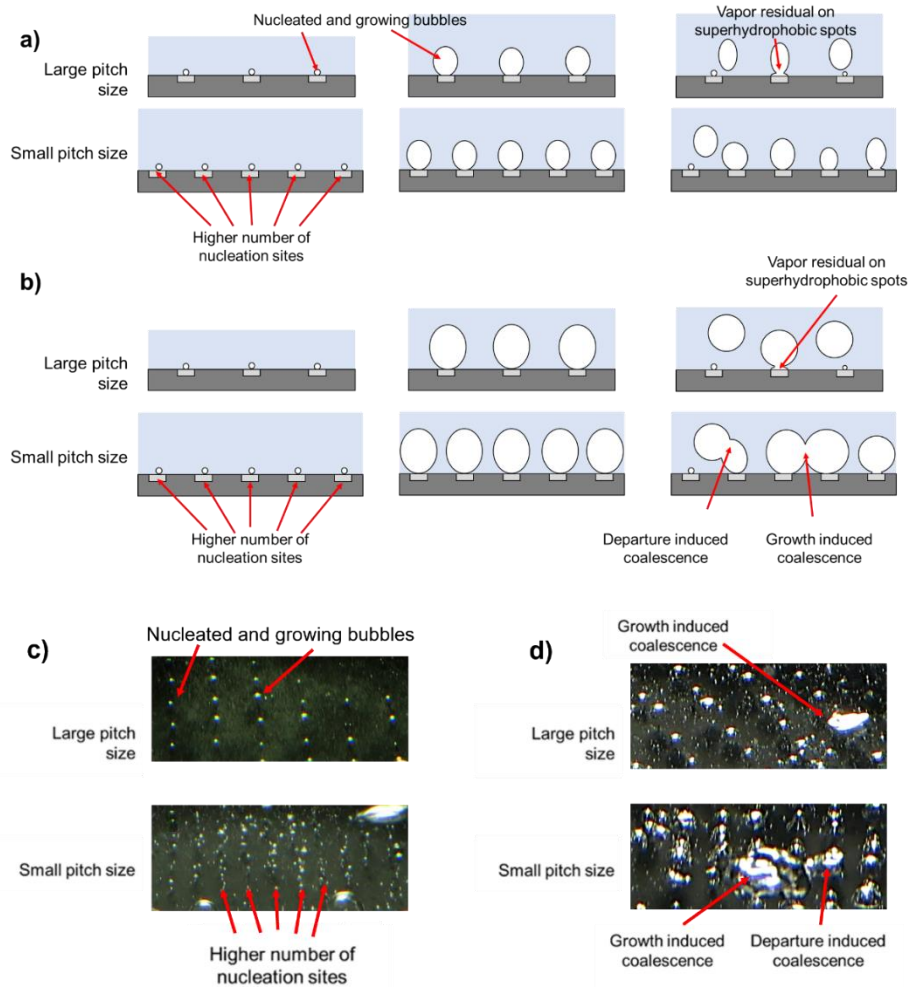
Figure 29 Schematic of nucleated and departed bubbles on superbiphilic surfaces at a)
atmospheric, b) sub-atmospheric pressure, and Boiling images c) atmospheric pressure
and lower heat flux, d) sub-atmospheric pressure and lower heat flux.

As seen in Figure 30, few nucleation sites on the superhydrophilic surface can be identified at low heat fluxes. However, at the same heat flux (16.3 kW/m^2), the superhydrophobic surface has a higher number of active nucleation sites, followed by the superhydrophobic spots on the superbiphilic surfaces. Thus, bubble nucleation on the superhydrophobic surface can be detected even at low heat fluxes. However, a delay in the onset of nucleate boiling (ONB) is observed on the superhydrophilic surface, which was also reported in the literature [83]. Furthermore, a large number of departed bubbles from the surface are visible, resulting in a significant number of vapor columns on the surface. Upon bubble departure, bubble recirculation can be detected for all the surfaces at higher heat fluxes. The superbiphilic surface with a low ratio of superhydrophobic area to the total surface area (<30%) provides a significant enhancement in boiling heat

transfer, by facilitating bubble generation on superhydrophobic spots and avoiding bubble coalescence as well. Additionally, remaining vapor upon bubble departure was evident on superhydrophobic spots, which were also observed in the literature [48,84]. These remaining vapor residuals serve as locations of further nucleation, resulting in the continuous growth and departure of new bubbles. Here, the superbiphilic surfaces enable continuous bubble departure from surfaces with a more uniform bubble departure size. On the other hand, a larger bubble departure diameter can be observed on the superhydrophobic surface (Sample #2) at high heat fluxes due to intense bubble coalescence, which results in deterioration in the heat transfer performance at sub-atmospheric pressure (28.3 kPa).
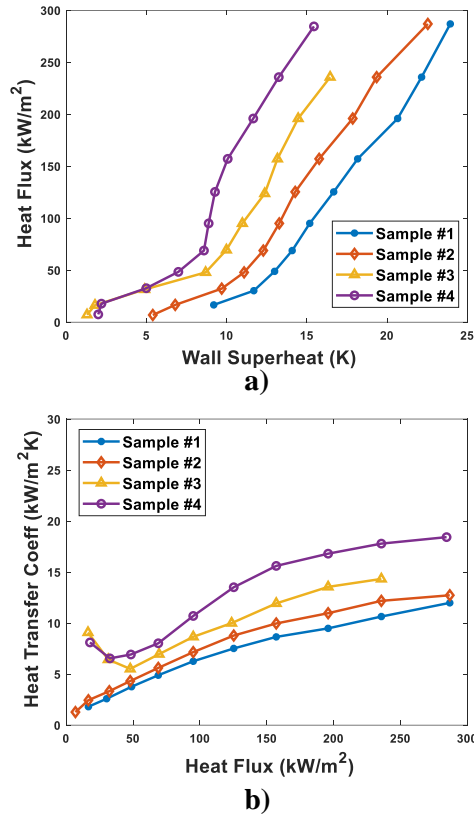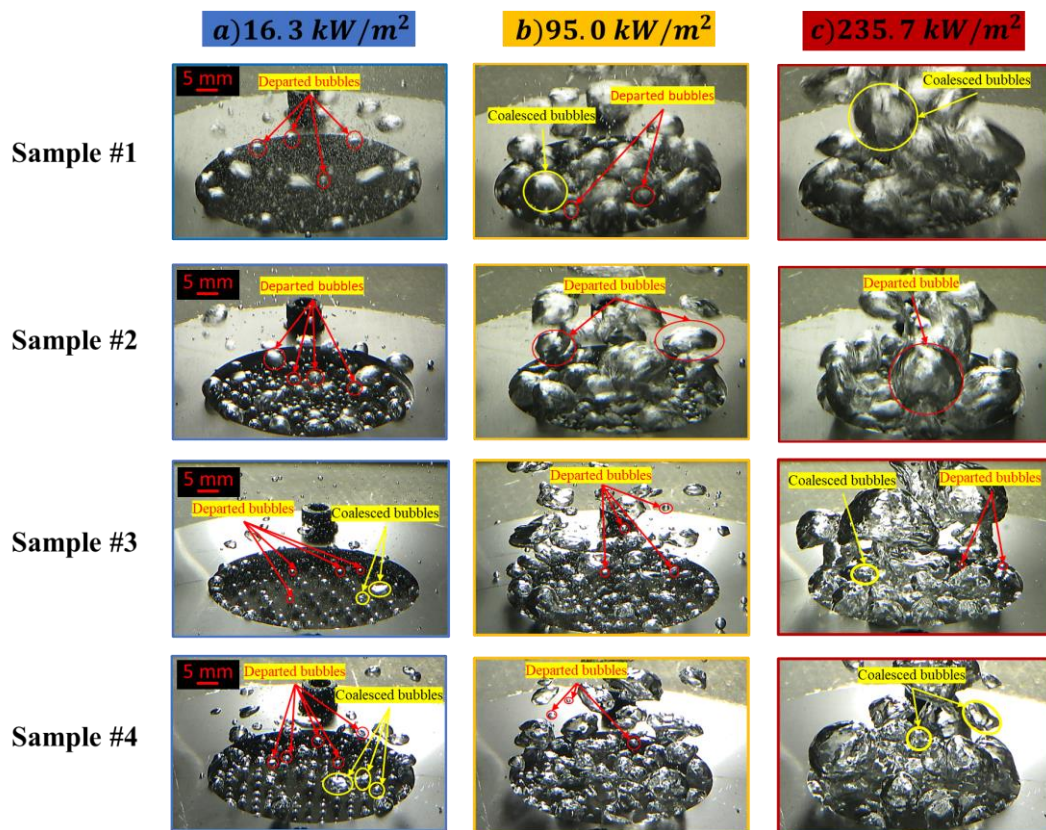

Figure 30 Boiling images corresponding to the homogenous superhydrophilic surface (Sample #1), homogenous superhydrophobic surface (Sample #2), superbiphilic surface with a diameter of 0.7 mm and pitch size of 5 mm (Sample #3), superbiphilic surface with a diameter of 0.7 mm and pitch size of 3 mm (Sample #4) at sub-atmospheric pressure (28.3 kPa) a) low heat flux, b) moderate heat flux, and c) high heat flux.

3.5.3. Comparison of the boiling heat transfer performance between atmospheric and sub-atmospheric pressures

The obtained results indicate a change in nucleated and departed bubble sizes between atmospheric and sub-atmospheric pressures (Figure 27 and Figure 30). On homogeneous surfaces, in contrast to very low pressures (i.e., <10kPa) where orders of magnitude changes in bubble size are reported, only an order of magnitude reduction in bubble size was observed with system pressure under the experimental conditions. This is in parallel with the reported studies in the literature [85]. Even though lateral coalescence of departing bubbles with adjacent bubbles can be observed at both atmospheric and sub-atmospheric pressures, bubble diameters are still significantly different at both pressures for Samples #1 and #2. A more evident decrease in the bubble diameter with the pressure increment can be seen for the superhydrophobic (Sample #2) surface. At low heat fluxes, smaller emerging bubbles result in a delay in bubble coalescence at atmospheric pressure. At higher heat fluxes, an increasing trend in the bubble departure diameter exists for the sub-atmospheric pressure (28.3 kPa), while almost a weaker trend in the diameter with wall heat flux is obtained at atmospheric pressure (103.7 kPa). This is also due to corresponding differences in nucleation and boiling physics at atmospheric and sub-atmospheric pressures. For instance, a wall heat flux of 95 kW/m^2 at sub-atmospheric pressure corresponds to slugs and vapor columns (developed nucleate boiling), while isolated bubbles are still evident on the heated surface at atmospheric pressure. As stated earlier, the superhydrophobic surface eliminates bubble nucleation waiting time at both pressures. The synergic effect of the corresponding nucleation, bubble coalescence, oblate shape bubbles, and lack of nucleation waiting time are the main reasons for considerably larger bubble departure diameters at medium/high heat fluxes for the homogenous superhydrophobic surface (Sample #2) at sub-atmospheric pressure compared to atmospheric pressure. However, the bubble departure diameter decreases with pressure increment for superbiphilic (Sample #3 and #4) surfaces at higher heat fluxes.

The comparison between obtained boiling HTCs at atmospheric (103.7 kPa) and sub-atmospheric (28.3 kPa) pressures are presented in Figure 31. Superbiphilic surfaces take the advantage of both superhydrophobic (earlier ONB and lower contact diameter) and superhydrophilic (lower departure diameter) surfaces and therefore provide higher

boiling HTCs compared to homogeneous samples (Samples#1 and #2). The superbiphilic surface with a pitch size of 3 mm and a diameter of 0.7 mm (Sample #4) has higher performance compared to the one with a pitch size of 5mm. A smaller difference in boiling heat transfer between Samples #3 and #4 at atmospheric pressure indicates the negligible role of the pitch size on bubble dynamics for the configurations studies in this study (pitch sizes of 3 and 5mm). The larger number of active nucleation sites at sub-atmospheric pressure could be the reason for the higher heat transfer performance for Sample #4 compared to Sample#3. Also, since bubble coalescence is more likely to occur at sub-atmospheric pressures, the enhancing effect of superbiphilicity on boiling heat transfer is more dominant for atmospheric pressures. In other words, the enhancements in boiling heat transfer with superbiphilicity are more significant for atmospheric pressure than sub-atmospheric pressures.
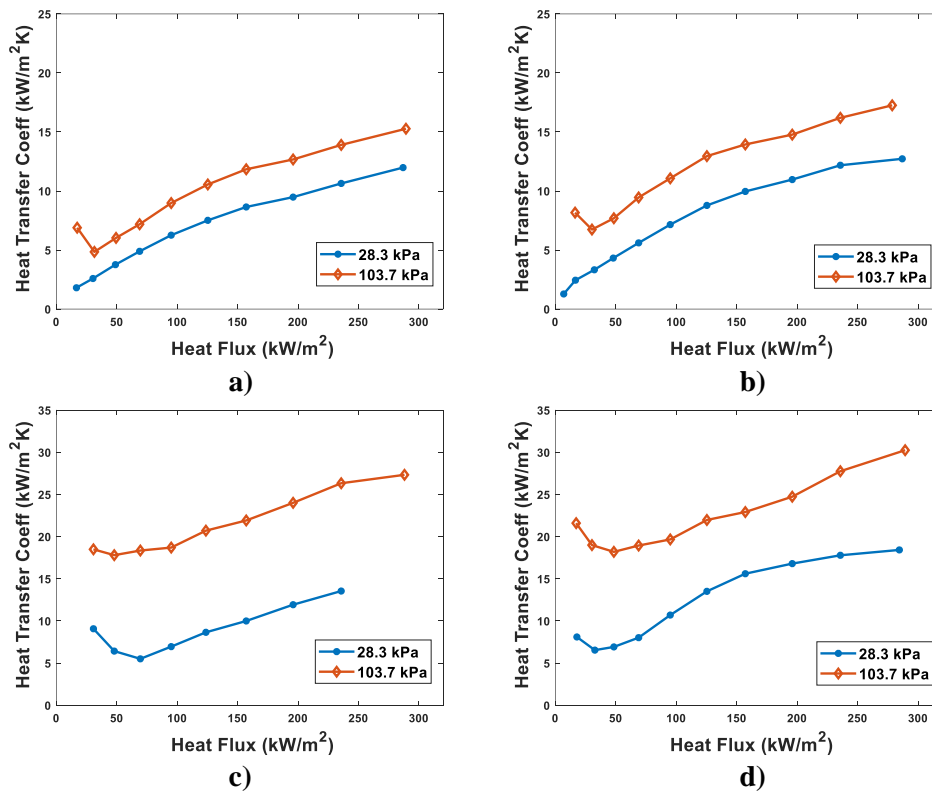
Figure 31 Comparison of HTCs at atmospheric and sub-atmospheric pressures a) superhydrophilic (Sample #1), b) superhydrophobic (Sample #2), c) superbiphilic surface with a spot diameter of 0.7 mm and pitch size of 5 mm (Sample #3), and d) superbiphilic surface with a spot diameter of 0.7 mm and pitch size of 3 mm (Sample #4).

4.   CHAPTER 4: CONCLUSIONS

In first this study, the effect of pin fins, tip clearance, and distribution pin fins on flow boiling heat transfer were investigated with the help of flow visualization efforts. The main conclusions drawn from this study can be summarized as follows:

- Heat transfer enhancements can be achieved with the use of elliptical pin fins compared to a plain channel configuration.
- Distribution pin fins can further augment heat transfer, which is linked with homogenous flow distribution and blockage of vapor phase to the inlet. Local heat spreading from elliptical pin fins to inlet zones results enhancement in heat transfer due to the larger planar extensions with presence of distribution pin fins at the inlet region.
- The heat sink with elliptical pin fins of no tip clearance and distribution pin fins has the best performance. Maximum heat transfer enhancement of over 35% relative to the plane channel heat sink can be achieved with this configuration, even though the plain channel heat sink operates at a 1.6 times larger mass flow rate for the same mass flux.
- Heat transfer coefficient increases with the mass flux, implying the effect of convective boiling, which is supported with intermittent and annular flows pattern along a significant portion of channel at the lowest mass flux and near the outlet at the highest mass flux.
- Regarding flow pattern maps, flow patterns shift to a more upstream location with heat flux, while the transitions between the flow patterns shift towards the exit of the channel with mass flux. The transition between flow patterns is delayed with the presence of pin fins.

In second study, an experimental investigation was performed to reveal the effect of surface modification and mixed wettability on the pool boiling performance at atmospheric and sub-atmospheric pressures using deionized water as the working fluid. One homogenous superhydophilic surface sample (Sample #1), one superhydrophobic surface sample (Sample #2), and two superbiphilic surface samples (with superhydrophobic area to the total area ratios of 11.30% and 28.31%) were tested. The

main conclusions from this study can be summarized as follows:

- The superbiphilic surface with a pitch size of 3 mm and superhydrophobic spots with a diameter of 0.7 mm (Sample #4) had the best performance at both atmospheric (103.7 kPa) and sub-atmospheric (28.3 kPa) pressures. Compared to the reference superhydrophilic surface, the boiling heat transfer coefficient enhancements up to 98% and 54% were achieved for atmospheric and sub-atmospheric pressures, respectively.

- The superhydrophobic island pitch size had a negligible effect on boiling heat transfer at atmospheric pressure. On the other hand, a large number of active nucleated bubbles at sub-atmospheric pressure resulted in boiling heat transfer enhancement on the superbiphilic surface with a smaller pitch size.

- A larger number of nucleation sites (at low wall heat fluxes) and coalescence induced bubble departure process (at medium heat fluxes) results in higher heat transfer coefficients on the superbiphilic surfaces compared to homogenous surfaces under sub-atmospheric conditions.

- The superhydrophobic (Sample #2) surface and superhydrophobic spots on the superbiphilic surfaces offer continuous bubble generation without the bubble nucleation waiting stage.

- The bubble departure diameter significantly increases upon a reduction in pressure on the homogenous superhydrophobic surface (at high heat fluxes).

- The superhydrophobic spots on superbiphilic surfaces behave as active nucleation sites at both atmospheric and sub-atmospheric pressures. Although a significant number of active nucleation sites can be seen on the homogenous superhydrophobic (Sample #2) surface, more enhancements in boiling heat transfer can be achieved on the superbiphilic (Sample #3 and #4) surfaces due to delays in bubble coalescence before the bubble departure.

5.   CHAPTER 5: FUTURE WORKS

Suggested future research directions for the first study can be summarized as:

- Hydrodynamic aspects can be presented for each configuration.
- Refrigerants, such as HFE – 7000 refrigerant, could be tested at different mass fluxes to reveal the effect of working fluid. This study can be extended to CHF (critical heat flux) condition.
- The experiments can be performed using different shapes of pin fins (such as triangular, square, etc.) to reveal the effect of pin fin shape.
- The experiments can be performed for the coated configurations with mixed wettability to reveal surface wettability effect.

Future research directions for the second study are listed as:

- The experiments can be performed using various functional surfaces with different pitch sizes and diameters of superhydrophobic spots to reveal optimum ratio under sub-atmospheric conditions.
- The experiments can be performed using different working fluids (such as HFE 7000, 7100, etc.) to reveal effect of working fluid.
- The experiments can be performed until the CHF condition to reveal the effect of surface modifications on CHF.
- The experiments can be performed at different sub-atmospheric pressure levels.

REFERENCES

[1]   H.E. Ahmed, B.H. Salman, A.S. Kherbeet, M.I. Ahmed, Optimization of thermal design of heat sinks: A review, Int. J. Heat Mass Transf. 118 (2018) 129–153. https://doi.org/10.1016/j.ijheatmasstransfer.2017.10.099.

[2]   T. Dixit, I. Ghosh, Review of micro- and mini-channel heat sinks and heat exchangers for single phase fluids, Renew. Sustain. Energy Rev. 41 (2015) 1298–1311. https://doi.org/10.1016/j.rser.2014.09.024.

[3]   W. Qu, I. Mudawar, Flow boiling heat transfer in two-phase micro-channel heat sinks-I. Experimental investigation and assessment of correlation methods, Int. J. Heat Mass Transf. 46 (2003) 2755–2771. https://doi.org/10.1016/S0017-9310(03)00041-3.

[4]   T. Chen, S. V. Garimella, Measurements and high-speed visualizations of flow boiling of a dielectric fluid in a silicon microchannel heat sink, Int. J. Multiph. Flow. 32 (2006) 957–971. https://doi.org/10.1016/j.ijmultiphaseflow.2006.03.002.

[5]   K.M. Jung, A. Krishnan R, U. Kumar G, H.J. Lee, Experimental study on two-phase pressure drop and flow boiling heat transfer in a micro pin fin channel heat sink under constant heat flux, Exp. Heat Transf. 34 (2021) 162–185. https://doi.org/10.1080/08916152.2020.1725182.

[6]   T. Alam, P.S. Lee, C.R. Yap, L. Jin, A comparative study of flow boiling heat transfer and pressure drop characteristics in microgap and microchannel heat sink and an evaluation of microgap heat sink for hotspot mitigation, Int. J. Heat Mass Transf.   58   (2013)   335–347. https://doi.org/10.1016/j.ijheatmasstransfer.2012.11.020.

[7]   Y.T. Jia, G.D. Xia, L.X. Zong, D.D. Ma, Y.X. Tang, A comparative study of experimental flow boiling heat transfer and pressure drop characteristics in porous-wall microchannel heat sink, Int. J. Heat Mass Transf. 127 (2018) 818–833. https://doi.org/10.1016/j.ijheatmasstransfer.2018.06.090.

[8]   D.D. Ma, G.D. Xia, L.X. Zong, Y.T. Jia, Y.X. Tang, R.P. Zhi, Experimental investigation of flow boiling heat transfer performance in zigzag microchannel heat sink for electronic cooling devices, Int. J. Therm. Sci. 145 (2019).

https://doi.org/10.1016/j.ijthermalsci.2019.106003.

[9]   M. Shojaeian, A. Koşar, Pool boiling and flow boiling on micro-and nanostructured surfaces, Exp. Therm. Fluid Sci. 63 (2015) 45–73.

[10]   Y. Şişman, A.K. Sadaghiani, K.R. Khedir, M. Brozak, T. Karabacak, A. Koşar, Subcooled Flow Boiling Over Microstructured Plates In Rectangular Minichannels, Nanoscale Microscale Thermophys. Eng. 20 (2016) 173–190. https://doi.org/10.1080/15567265.2016.1248584.

[11]   D. Deng, W. Wan, Y. Qin, J. Zhang, X. Chu, Flow boiling enhancement of structured microchannels with micro pin fins, Int. J. Heat Mass Transf. 105 (2017) 338–349. https://doi.org/10.1016/j.ijheatmasstransfer.2016.09.086.

[12]   A. Reeser, A. Bar-Cohen, G. Hetsroni, High quality flow boiling heat transfer and pressure drop in microgap pin fin arrays, Int. J. Heat Mass Transf. 78 (2014) 974–985. https://doi.org/10.1016/j.ijheatmasstransfer.2014.05.021.

[13]   F. Xu, H. Wu, Z. Liu, Flow patterns during flow boiling instability in silicon-based pin-fin microchannels, J. Heat Transfer. 140 (2018) 1–10. https://doi.org/10.1115/1.4038194.

[14]   B. Parizad Benam, A.K. Sadaghiani, V. Yağcı, M. Parlak, K. Sefiane, A. Koşar, Review on high heat flux flow boiling of refrigerants and water for electronics cooling, Int. J. Heat Mass Transf. 180 (2021) 121787. https://doi.org/10.1016/J.IJHEATMASSTRANSFER.2021.121787.

[15]   A. Mohammadi, A. Koşar, Review on Heat and Fluid Flow in Micro Pin Fin Heat Sinks under Single-phase and Two-phase Flow Conditions, Nanoscale Microscale Thermophys. Eng. 22 (2018) 153–197. https://doi.org/10.1080/15567265.2018.1475525.

[16]   J. Zhao, S. Huang, L. Gong, Z. Huang, Numerical study and optimizing on micro square pin-fin heat sink for electronic cooling, Appl. Therm. Eng. 93 (2016) 1347–1359. https://doi.org/10.1016/J.APPLTHERMALENG.2015.08.105.

[17]   A. Mohammadi, A. Koşar, The effect of arrangement type and pitch ratio on the performance of micro-pin-fin heat sinks, J. Therm. Anal. Calorim. 140 (2020) 1057–1068. https://doi.org/10.1007/s10973-019-08840-2.

[18]   W. Wan, D. Deng, Q. Huang, T. Zeng, Y. Huang, Experimental study and optimization of pin fin shapes in flow boiling of micro pin fin heat sinks, Appl. Therm. Eng. 114 (2017) 436–449.

https://doi.org/10.1016/j.applthermaleng.2016.11.182.

[19]   S.G. Kandlikar, Heat transfer mechanisms during flow boiling in microchannels, J. Heat Transfer. 126 (2004) 8–16. https://doi.org/10.1115/1.1643090.

[20]   D. SOODPHAKDEE, M. BEHNIA, D. COPELAND, A comparison of fin geometries for heatsinks in laminar forced convection: Part I - Round, elliptical, and plate fins in staggered and in-line configurations, Int. J. Microcircuits Electron. Packag. 24 (2001) 68–76.

[21]   A. Arshad, H.M. Ali, S. Khushnood, M. Jabbal, Experimental investigation of PCM based round pin-fin heat sinks for thermal management of electronics: Effect of pin-fin diameter, Int. J. Heat Mass Transf. 117 (2018) 861–872. https://doi.org/10.1016/j.ijheatmasstransfer.2017.10.008.

[22]   H.M. Ali, A. Arshad, M. Jabbal, P.G. Verdin, Thermal management of electronics devices with PCMs filled pin-fin heat sinks: A comparison, Int. J. Heat Mass Transf. 117 (2018) 1199–1204. https://doi.org/10.1016/j.ijheatmasstransfer.2017.10.065.

[23]   T. Ambreen, A. Saleem, C.W. Park, Pin-fin shape-dependent heat transfer and fluid flow characteristics of water- and nanofluid-cooled micropin-fin heat sinks: Square, circular and triangular fin cross-sections, Appl. Therm. Eng. 158 (2019) 113781. https://doi.org/10.1016/j.applthermaleng.2019.113781.

[24]   T. Ambreen, M.H. Kim, Effect of fin shape on the thermal performance of nanofluid-cooled micro pin-fin heat sinks, Int. J. Heat Mass Transf. 126 (2018) 245–256. https://doi.org/10.1016/j.ijheatmasstransfer.2018.05.164.

[25]   R. Ricci, S. Montelpare, An experimental IR thermographic method for the evaluation of the heat transfer coefficient of liquid-cooled short pin fins arranged in line, Exp. Therm. Fluid Sci. 30 (2006) 381–391. https://doi.org/10.1016/J.EXPTHERMFLUSCI.2005.09.004.

[26]   A. Koşar, Y. Peles, TCPT-2006-096.R2: Micro scale pin fin heat sinks - Parametric performance evaluation study, IEEE Trans. Components Packag. Technol. 30 (2007) 855–865. https://doi.org/10.1109/TCAPT.2007.906334.

[27]   W. Bai, D. Liang, W. Chen, M.K. Chyu, Investigation of ribs disturbed entrance effect of heat transfer and pressure drop in pin-fin array, Appl. Therm. Eng. 162 (2019) 114214. https://doi.org/10.1016/J.APPLTHERMALENG.2019.114214.

[28]   A.K. Sadaghiani, A. Koşar, Experimental Study on Subcooled Flow Boiling in

Horizontal Microtubes and Effect of Heated Length, Heat Transf. Eng. 38 (2017) 313–322. https://doi.org/10.1080/01457632.2016.1189270.

[29] T. Izci, M. Koz, A. Koşar, The effect of micro pin-fin shape on thermal and hydraulic performance of micro pin-fin heat sinks, Heat Transf. Eng. 36 (2015) 1447–1457. https://doi.org/10.1080/01457632.2015.1010921.

[30] D. Deng, L. Zeng, W. Sun, G. Pi, Y. Yang, Experimental study of flow boiling performance of open-ring pin fin microchannels, Int. J. Heat Mass Transf. 167 (2021) 120829. https://doi.org/10.1016/j.ijheatmasstransfer.2020.120829.

[31] M. Parlak, A. Özsunar, A. Koşar, High aspect ratio microchannel heat sink optimization under thermally developing flow conditions based on minimum power consumption, Appl. Therm. Eng. 201 (2022). https://doi.org/10.1016/j.applthermaleng.2021.117700.

[32] J. Pandit, M. Thompson, S. V. Ekkad, S.T. Huxtable, Effect of pin fin to channel height ratio and pin fin geometry on heat transfer performance for flow in rectangular channels, Int. J. Heat Mass Transf. 77 (2014) 359–368. https://doi.org/10.1016/j.ijheatmasstransfer.2014.05.030.

[33] Y.J. Lee, S.J. Kim, Thermal optimization of the pin-fin heat sink with variable fin density cooled by natural convection, Appl. Therm. Eng. 190 (2021) 116692. https://doi.org/10.1016/J.APPLTHERMALENG.2021.116692.

[34] S.W. Chang, P.S. Wu, W.L. Cai, C.H. Yu, Experimental heat transfer and flow simulations of rectangular channel with twisted-tape pin-fin array, Int. J. Heat Mass Transf. 166 (2021) 120809. https://doi.org/10.1016/J.IJHEATMASSTRANSFER.2020.120809.

[35] C.H. Huang, Y.R. Huang, An optimum design problem in estimating the shape of perforated pins and splitters in a plate-pin-fin heat sink, Int. J. Therm. Sci. 170 (2021) 107096. https://doi.org/10.1016/J.IJTHERMALSCI.2021.107096.

[36] S.C. Hung, S.C. Huang, Y.H. Liu, Effect of nonuniform pin size on heat transfer in a rotating rectangular channel with pin-fin arrays, Appl. Therm. Eng. 163 (2019) 114393. https://doi.org/10.1016/J.APPLTHERMALENG.2019.114393.

[37] Z.G. Liu, N. Guan, C.W. Zhang, G.L. Jiang, The Flow Resistance and Heat Transfer Characteristics of Micro Pin-Fins with Different Cross-Sectional Shapes, (2015). https://doi.org/10.1080/15567265.2015.1073820.

[38] F. Xu, H. Wu, Effect of pin-fins on the onset of flow instability of water in silicon-

based microgap, Int. J. Therm. Sci. 130 (2018) 496–506. https://doi.org/10.1016/J.IJTHERMALSCI.2018.05.020.

[39] S.J. Kim, D. Kim, Forced Convection in Microstructures for Electronic Equipment Cooling, J. Heat Transfer. 121 (1999) 639–645. https://doi.org/10.1115/1.2826027.

[40] S.J.K. J.H. Ryu, D.H. Choi, Numerical optimization of the thermal performance of a microchannel heat sink, (2002).

[41] S.K. Krishnababu, P.J. Newton, W.N. Dawes, G.D. Lock, H.P. Hodson, J. Hannis, C. Whitney, Aerothermal investigations of tip leakage flow in axial flow turbines-part i: Effect of tip geometry and tip clearance gap, J. Turbomach. 131 (2009) 1–14. https://doi.org/10.1115/1.2950068.

[42] J.Y. Min, S.P. Jang, S.J. Kim, Effect of tip clearance on the cooling performance of a microchannel heat sink, Int. J. Heat Mass Transf. 47 (2004) 1099–1103. https://doi.org/10.1016/j.ijheatmasstransfer.2003.08.020.

[43] K.A. Moores, Y.K. Joshi, Effect of tip clearance on the thermal and hydrodynamic performance of a shrouded pin fin array, J. Heat Transfer. 125 (2003) 999–1006. https://doi.org/10.1115/1.1621897.

[44] A. Shahsavar, M. Shahmohammadi, I.B. Askari, CFD simulation of the impact of tip clearance on the hydrothermal performance and entropy generation of a water-cooled pin-fin heat sink, Int. Commun. Heat Mass Transf. 126 (2021) 105400. https://doi.org/10.1016/J.ICHEATMASSTRANSFER.2021.105400.

[45] L.H. Chien, R.L. Webb, A nucleate boiling model for structured enhanced surfaces, Int. J. Heat Mass Transf. 41 (1998) 2183–2195. https://doi.org/10.1016/S0017-9310(97)00302-5.

[46] A. Surtaev, D. Kuznetsov, V. Serdyukov, A. Pavlenko, V. Kalita, D. Komlev, A. Ivannikov, A. Radyuk, Structured capillary-porous coatings for enhancement of heat transfer at pool boiling, Appl. Therm. Eng. 133 (2018) 532–542. https://doi.org/10.1016/j.applthermaleng.2018.01.051.

[47] C. Huh, L.E. Scriven, Hydrodynamic model of steady movement of a solid/liquid/fluid contact line, J. Colloid Interface Sci. 35 (1971) 85–101. https://doi.org/10.1016/0021-9797(71)90188-3.

[48] V. Serdyukov, G. Patrin, I. Malakhov, A. Surtaev, Biphilic surface to improve and stabilize pool boiling in vacuum, Appl. Therm. Eng. 209 (2022) 118298.

https://doi.org/10.1016/J.APPLTHERMALENG.2022.118298.

[49] A. Surtaev, V. Serdyukov, I. Malakhov, Effect of subatmospheric pressures on heat transfer, vapor bubbles and dry spots evolution during water boiling, Exp. Therm. Fluid Sci. 112 (2020) 109974. https://doi.org/10.1016/J.EXPTHERMFLUSCI.2019.109974.

[50] C.C. Hsu, P.H. Chen, Surface wettability effects on critical heat flux of boiling heat transfer using nanoparticle coatings, Int. J. Heat Mass Transf. 55 (2012) 3713–3719. https://doi.org/10.1016/J.IJHEATMASSTRANSFER.2012.03.003.

[51] A.R. Betz, J. Jenkins, C.J. Kim, D. Attinger, Boiling heat transfer on superhydrophilic, superhydrophobic, and superbiphilic surfaces, Int. J. Heat Mass Transf. 57 (2013) 733–741. https://doi.org/10.1016/J.IJHEATMASSTRANSFER.2012.10.080.

[52] A. Surtaev, A. Koşar, V. Serdyukov, I. Malakhov, Boiling at subatmospheric pressures on hydrophobic surface: Bubble dynamics and heat transfer, Int. J. Therm. Sci. 173 (2022) 107423. https://doi.org/10.1016/J.IJTHERMALSCI.2021.107423.

[53] A.R. Motezakker, A.K. Sadaghiani, S. Çelik, T. Larsen, L.G. Villanueva, A. Koşar, Optimum ratio of hydrophobic to hydrophilic areas of biphilic surfaces in thermal fluid systems involving boiling, Int. J. Heat Mass Transf. 135 (2019) 164–174. https://doi.org/10.1016/J.IJHEATMASSTRANSFER.2019.01.139.

[54] V.E. Ahmadi, A. Aboubakri, A.K. Sadaghiani, K. Sefiane, A.K. Ko¸sar, Effect of Functional Surfaces with Gradient Mixed Wettability on Flow Boiling in a High Aspect Ratio Microchannel, (2020). https://doi.org/10.3390/fluids5040239.

[55] H.-C. Cheng, Z.-X. Jiang, T.-L. Chang, P.-H. Chen, Effects of difference in wettability level of biphilic patterns on copper tubes in pool boiling heat transfer, Exp. Therm. Fluid Sci. 120 (2021) 110241. https://doi.org/10.1016/j.expthermflusci.2020.110241.

[56] M. Zupančič, M. Steinbücher, P. Gregorčič, I. Golobič, Enhanced pool-boiling heat transfer on laser-made hydrophobic/superhydrophilic polydimethylsiloxane-silica patterned surfaces, Appl. Therm. Eng. 91 (2015) 288–297. https://doi.org/10.1016/J.APPLTHERMALENG.2015.08.026.

[57] Z.H. Liu, X.F. Yang, J.G. Xiong, Boiling characteristics of carbon nanotube suspensions under sub-atmospheric pressures, Int. J. Therm. Sci. 49 (2010) 1156–

1164. https://doi.org/10.1016/J.IJTHERMALSCI.2010.01.023.

[58]   M. Arya, · Sameer Khandekar, · Dheeraj Pratap, · S Anantha Ramakrishna, S. Khandekar, Pool boiling of water on nano-structured micro wires at sub-atmospheric conditions, Heat Mass Transf. 52 (2016) 1725–1737. https://doi.org/10.1007/s00231-015-1692-2.

[59]   Y. Takata, S. Hidaka, M. Masuda, T. Ito, Pool boiling on a superhydrophilic surface, Int. J. ENERGY Res. Int. J. Energy Res. 27 (2003) 111–119. https://doi.org/10.1002/er.861.

[60]   H.T. Phan, N. Caney, P. Marty, S. Colasson, J. Gavillet, Surface wettability control by nanocoating: The effects on pool boiling heat transfer and nucleation mechanism, Int. J. Heat Mass Transf. 52 (2009) 5459–5471. https://doi.org/10.1016/J.IJHEATMASSTRANSFER.2009.06.032.

[61]   M. Yamada, B. Shen, T. Imamura, S. Hidaka, M. Kohno, K. Takahashi, Y. Takata, Enhancement of boiling heat transfer under sub-atmospheric pressures using biphilic surfaces, Int. J. Heat Mass Transf. 115 (2017) 753–762. https://doi.org/10.1016/J.IJHEATMASSTRANSFER.2017.08.078.

[62]   C.H. Wang, V.K. Dhir, Effect of Surface Wettability on Active Nucleation Site Density During Pool Boiling of Water on a Vertical Surface, J. Heat Transfer. 115 (1993) 659–669. https://doi.org/10.1115/1.2910737.

[63]   H. Demir, M. Mobedi, S. Ülkü, A review on adsorption heat pump: Problems and solutions, Renew. Sustain. Energy Rev. 12 (2008) 2381–2403. https://doi.org/10.1016/J.RSER.2007.06.005.

[64]   A.D. Khawaji, I.K. Kutubkhanah, J.M. Wie, Advances in seawater desalination technologies, Desalination. 221 (2008) 47–69. https://doi.org/10.1016/J.DESAL.2007.01.067.

[65]   S. Chuang, G. Dong, Z. Wang, S. Fengxian, Investigation on Active Thermal Control Method with Pool Boiling Heat Transfer at Low Pressure, J. Therm. Sci. 27 (2018) 277–284. https://doi.org/10.1007/s11630-018-1009-0.

[66]   A. Kalani, S.G. Kandlikar, Enhanced pool boiling with ethanol at subatmospheric pressures for electronics cooling, J. Heat Transfer. 135 (2013). https://doi.org/10.1115/1.4024595.

[67]   T. Baki, Boiling Pure Fluids at Sub Atmospheric Pressures Simulation of bubble growth View project Influence of Operational Parameters on the Statistics of

Thermal Field in Low Damköhler Reaction Zones View project, n.d.

[68] R. Volmer, J. Eckert, G. Füldner, L. Schnabel, Evaporator development for adsorption heat transformation devices – Influencing factors on non-stationary evaporation with tube-fin heat exchangers at sub-atmospheric pressure, Renew. Energy. 110 (2017) 141–153. https://doi.org/10.1016/J.RENENE.2016.08.030.

[69] S.K. Singh, D. Sharma, Review of pool and flow boiling heat transfer enhancement through surface modification, Int. J. Heat Mass Transf. 181 (2021) 122020. https://doi.org/10.1016/J.IJHEATMASSTRANSFER.2021.122020.

[70] H.M. Ali, W. Arshad, Thermal performance investigation of staggered and inline pin fin heat sinks using water based rutile and anatase TiO2 nanofluids, Energy Convers. Manag. 106 (2015) 793–803. https://doi.org/10.1016/j.enconman.2015.10.015.

[71] Y. Wang, F. Houshmand, D. Elcock, Y. Peles, Convective heat transfer and mixing enhancement in a microchannel with a pillar, Int. J. Heat Mass Transf. 62 (2013) 553–561. https://doi.org/10.1016/j.ijheatmasstransfer.2013.03.034.

[72] D. Mei, X. Lou, M. Qian, Z. Yao, L. Liang, Z. Chen, Effect of tip clearance on the heat transfer and pressure drop performance in the micro-reactor with micro-pin-fin arrays at low Reynolds number, Int. J. Heat Mass Transf. 70 (2014) 709–718. https://doi.org/10.1016/j.ijheatmasstransfer.2013.11.060.

[73] W. Coleman, W. Glenn Steck, J. Wiley, Experimentation, validation, and uncertainty analysis for engineers, Prentice-Hall, Inc, 2018.

[74] R. Shah, A. London, Laminar flow forced convection in ducts: a source book for compact heat exchanger analytical data, 2014.

[75] M.I. Hasan, Investigation of flow and heat transfer characteristics in micro pin fin heat sink with nanofluid, Appl. Therm. Eng. 63 (2014) 598–607. https://doi.org/10.1016/j.applthermaleng.2013.11.059.

[76] T. Yeom, T. Simon, T. Zhang, M. Zhang, … M.N.-I.J. of, undefined 2016, Enhanced heat transfer of heat sink channels with micro pin fin roughened walls, Elsevier. (n.d.).

[77] S. Krishnamurthy, Y. Peles, Flow boiling heat transfer on micro pin fins entrenched in a microchannel, J. Heat Transfer. 132 (2010) 1–10. https://doi.org/10.1115/1.4000878.

[78] A. Koşar, Y. Peles, Boiling heat transfer in a hydrofoil-based micro pin fin heat

sink, Int. J. Heat Mass Transf. 50 (2007) 1018–1034. https://doi.org/10.1016/j.ijheatmasstransfer.2006.07.032.

[79] G. Huang, K. Tang, S. Yu, Y. Tang, S. Zhang, Enhanced pool boiling heat transfer by metallic nanoporous surfaces under low pressure, Int. J. Heat Mass Transf. 184 (2022) 122382. https://doi.org/10.1016/J.IJHEATMASSTRANSFER.2021.122382.

[80] P. Gregorčič, B. Šetina-Batič, M. Hočevar, Controlling the stainless steel surface wettability by nanosecond direct laser texturing at high fluences, Appl. Phys. A Mater. Sci. Process. 123 (2017). https://doi.org/10.1007/s00339-017-1392-5.

[81] W.M. Rohsenow, P. Griffith, Correlation of maximum heat flux data for boiling of saturated liquids, Cambridge, Mass.: Massachusetts Institute of Technology, Division of …, 1955.

[82] H. Jo, H.S. Ahn, S. Kang, M.H. Kim, A study of nucleate boiling heat transfer on hydrophilic, hydrophobic and heterogeneous wetting surfaces, Int. J. Heat Mass Transf. 54 (2011) 5643–5652. https://doi.org/10.1016/j.ijheatmasstransfer.2011.06.001.

[83] B. Shen, M. Yamada, T. Mine, S. Hidaka, M. Kohno, K. Takahashi, Y. Takata, Depinning of bubble contact line on a biphilic surface in subatmospheric boiling: Revisiting the theories of bubble departure, Int. J. Heat Mass Transf. 126 (2018) 715–720. https://doi.org/10.1016/j.ijheatmasstransfer.2018.06.030.

[84] Y. Nam, J. Wu, G. Warrier, Y. Sungtaek Ju, Experimental and numerical study of single bubble dynamics on a hydrophobic surface, J. Heat Transfer. 131 (2009) 1–7. https://doi.org/10.1115/1.3216038.

[85] S. Michaie, R. Rullière, J. Bonjour, Experimental study of bubble dynamics of isolated bubbles in water pool boiling at subatmospheric pressures, Exp. Therm. Fluid Sci. 87 (2017) 117–128. https://doi.org/10.1016/j.expthermflusci.2017.04.030.